Acta Materialia 239 (2022) 118291

Contents lists available at ScienceDirect

Acta Materialia

journal homepage: www.elsevier.com/locate/actamat

Full length article

Ultrastrong and stress corrosion cracking-resistant martensitic steels

Sangeun Park[a], Jung Gi Kim[a], Im Doo Jung[b], Jae Bok Seol[a,**], Hyokyung Sung[a,c,*]

[a] Department of Materials Engineering and Convergence Technology, Center for K-metals, Gyeongsang National University, Jinju 52828, Republic of Korea
[b] Department of Mechanical Engineering, Ulsan National Institute of Science and Technology, Ulsan 44919, Republic of Korea
[c] Department of Materials Science and Engineering, Kookmin University, Seoul 02707, Republic of Korea

ARTICLE INFO

Article history:
Received 4 February 2022
Revised 18 August 2022
Accepted 20 August 2022
Available online 21 August 2022

Keywords:
High-strength steel
Martensite
Stress corrosion cracking
Grain boundary segregation

ABSTRACT

This study aims to reveal the atomic-scale effects of tempering on the complex substructures and stress corrosion cracking (SCC) resistance of high-strength martensitic steels. The SCC resistance and strength of boron-doped Fe-0.3C-0.3Si-1.0Mn-1.0Ni-0.5Cr (wt%) martensitic steel increase concurrently without low-temperature tempering. Notably, the degradation of SCC resistance caused by tempering is in contrast with the known effect. To explore this unexpected result, subboundaries inside the martensitic microstructure are investigated via atomic-nano-micro-scale analyses. The strongly segregated carbon at the lath boundaries during tempering is a precursor to the harmful cementite, which acts as severe SCC initiation sites. Eventually, intensive crack grew along the lath boundaries, deteriorating the SCC resistance of the material.

1. Introduction

Steels is still a major structural engineering material with an annual production exceeding 1.6 billion tons [1]. Displacive shear transformation from ductile face-centered-cubic (fcc) γ-austenite to strong body-centered-tetragonal (bct) α'-martensite in steels is a diffusionless process that occurs during heat treatments or deformation to generate high dislocation density. Therefore, martensitic steels are usually stronger than conventional transformation-induced plasticity (TRIP) and twinning-induced plasticity (TWIP) steels without grain refinement [2].

Ultrastrong martensitic steels require high sustainability [3,4] when exposed to extreme and harsh environments for aerospace and defense applications [5–8]. Stress corrosion cracking (SCC) is crucial for sustainability because it leads to the failure of martensitic steel structures [9–12]. The existence of high-density dislocation and high residual stress at internal martensitic microstructures degrades SCC resistance due to displacive shear transformation [13–16]. Furthermore, during tempering process of the martensitic steels, solute redistribution and resultant precipitation at grain boundaries (GBs) can deteriorate the SCC resistance [17,18]. Micro-voids and associated cracks are then formed in the vicinity of the harmful GB precipitates due to the corrosion potential gap between matrix and precipitates [19,20]. These efforts give indications that increasing the SCC resistance of martensitic steels without a loss in strength is a bit puzzling. In other words, overcoming the strength-SCC tradeoff enables the development of a wide range of ultrastrong martensitic steels with high sustainability.

Martensitic steels comprise hierarchical substructures, such as packets, blocks, and laths in one martensite grain surrounded by prior austenite grain boundaries (PAGB). Table 1 summarizes the boundary characteristics based on the misorientation angles among various subboundaries in martensitic substructures [21–25]. These subboundaries can be classified as low-angle grain boundaries (LAGBs) and high-angle grain boundaries (HAGBs) to distinguish their different impacts on deformation behavior. Such complicated microstructures substantially influence the mechanical properties and SCC susceptibility of the steels. Particular attention has been given to block boundaries, which are representative HAGB, for understanding the strengthening mechanism of the martensite phase [26–28]. Zhang et al. [29] proposed that the average block size was inversely proportional to yield strength, like the Hall–Petch relationship for grain size. Later, Ghassemi-Armaki et al. [30] performed micropillar compression tests where multiple block micropillars led to dramatic work hardening, and single block micropillars resulted in perfect elastic-plastic behavior. Furthermore,

* Corresponding author.
** Co-corresponding author.
E-mail addresses: jb.seol@gnu.ac.kr (J.B. Seol), hksung@gnu.ac.kr (H. Sung).

https://doi.org/10.1016/j.actamat.2022.118291

Table 1
Classification of martensite substructures by misorientation angle.

Misorientation angle (°)				
Lath boundary	Prior γ grain boundary	Packet boundary	Block boundary	Ref.
$0 < \theta < 15$	$10 < \theta < 55$		$55 < \theta$	[21]
$0 < \theta < 10.53$	$10.53 < \theta < 51.73$		$51.73 < \theta$	[22]
–	$15 < \theta < 45$		$45 < \theta < 65$	[23]
$\theta < 15$	$15 < \theta < 45$	$45 < \theta < 55$	$55 < \theta < 65$	[24]
$2.5 < \theta < 15$	Effective grain: $15 < \theta$			[25]

block size is regarded as the effective grain size of the martensite phase because block boundaries with misorientation angles > ~10.53° (belonging to the HAGB) inhibit the slip transfer [31,32].

The PAGB preferentially corrodes due to the presence of segregated solutes and carbides [33,34], playing an important role in the SCC property of steel. The PAGB segregation of alloying elements affects the differences in corrosion potential between the matrix and boundary, leading to intergranular fracture. Kadowaki et al. [35] proposed that for ferrite-pearlite carbon steel, pitting corrosion occurs in pearlite in a 0.1 M NaCl solution due to sulfur segregation. Mishra et al. [36] reported that grain boundary corrosion is enhanced by vacancies introduced due to oxidation of reactive Si atoms in a high-strength low alloy steel. Küpper et al. [37] revealed that small amounts of phosphorus (0.003–2.5 wt%) were mostly segregated along the PAGBs, stimulating the intergranular corrosion of Fe–P alloys. In addition, boron-free TWIP steel showed superior corrosion resistance (0.2 V higher E_{corr}) in the immersion test than boron-containing TWIP steel, wherein boron strongly segregated the PAGBs [38]. Due to high strain energy, complex interactions around boron-rich precipitates promoted electrochemical reactions in the boundary during strain-induced deformation. Despite intensive efforts, the effect of PAGB solute segregation on the strength-SCC trade-off of martensitic steels, including profuse boundaries (packet, blocs, and lath boundaries), is still unclear.

The tempering process leads to carbon redistribution and carbide formation in the vicinity of PAGBs and influences both properties, similar to PAGB segregation of alloying elements. Upon tempering, initial carbon clusters form due to thermal activity via spinodal decomposition and transform into transition carbides or cementites at the carbon-rich dislocation core [39–43]. The sizes and morphologies of the carbides and cementites resting on galvanic corrosion and stress concentration sites act as crack initiation sites for the martensitic steels [44–47]. Xue et al. [48] discovered that the composition of iron and silicon carbides contributed to the formation of pitting corrosion. Differences in the corrosion potential of the carbide and the matrix could create micro-crevices and localized stresses surrounding carbides [49–52]. The SCC behavior is affected by the change in local electrochemical properties resulting from localized stress at the interphase boundary between the matrix and the carbide. Therefore, uncovering the tempering effect on the microstructure, SCC properties, and mechanical properties of martensitic microstructure has recently become a critical issue. However, multiple-scale bridging analysis are required to fully understand any potential effect of solute redistribution on the complex martensitic microstructure including carbon and boron. Particularly, in-depth characterization of solute partitioning along the plentiful subboundaries after tempering is essential.

This study aims to reveal the effects of dislocation density, carbon segregation, and carbides on the tensile properties, corrosion, and SCC resistance of ultrastrong martensitic steels. These steels are subjected to experimentally multiscale characterization techniques from the micrometer to the atomic regime, focusing on misorientation angles and solute segregation at subboundaries. We show that the misorientation angles of such complicated subboundaries can be determined by a combined analysis of transmission Kikuchi diffraction (TKD) and transmission electron microscopy (TEM) measurements at the same positions in TEM specimens. To the best of our knowledge, no reports are available on a feasible route for identifying the misorientation angles of complex subboundaries for the martensitic microstructure in TEM images. The segregation of boron and carbon elements at the substantial boundaries observed using atom probe tomography (APT) also aided in confirming the atomic elemental effect on the SCC behavior of martensitic steels. Consequently, we can provide insights into the atomic scale effects of tempering on the corrosion and SCC resistance of ultrastrong martensitic steels that are designed to require high sustainability.

2. Experimental

Martensitic steel, with a chemical composition of Fe-0.3C-0.3Si-1.0Mn-1.0Ni-0.5Cr-0.003B (wt%), was prepared as an ingot using a high-frequency under a protective Ar atmosphere. The ingot was reheated at 1230 °C for 3.0 h and hot-rolled to obtain a 95% reduction from 120 to 6 mm in austenite single-phase area at approximately 870–900 °C, and quenched to obtain a quenched martensite microstructure. Tempered martensite specimens were normalized at 900 °C for 0.5 h, oil-quenched and tempered at 180 °C for 1.0 h, and air-cooled to room temperature. Hereafter, the water-quenched samples are denoted by QM, whereas the tempered martensite specimens are denoted by TM.

Rod-type tensile specimens were prepared with a gage length of 24 mm and a diameter of 4 mm in the longitudinal direction. Tensile curves were obtained using a uniaxial tension tensile testing machine (UT-100E, MTDI, Korea) following ASTM E8/E8M [53]. A 100 kN load cell operated at a strain rate of 10^{-3} s^{-1} was used for the tensile tests at room temperature of three specimens at each condition to confirm the reproducibility of the measurements.

The open circuit potential (OCP) and potentiodynamic polarization measurements were carried out using a potentiostat/galvanostat (WPG100, Won-A-Tech, Korea) according to ASTM G5 [54]. A three-electrode electrochemical cell was employed with the specimen as working electrode, Ag/AgCl (NaCl, 3 M) as the reference electrode, and graphite as the counter electrode. The specimen (working electrode) were immersed in the test solution for 60 min to obtain a stable OCP (E_{OC}). The corresponding E_{OC} vs. time curves are shown in Fig. 4(b); all potentiodynamic polarization tests were performed at a scan rate of 1 mV s^{-1} in 3.5% NaCl solution at room temperature. The electrochemical impedance spectroscopy (EIS) were performed using VMP3 potentiostat (Bio-Logic) and EC-Lab software (v 11.21) in 3.5 wt% NaCl solution at room temperature. For the measurements with an amplitude of 10 mV over a frequency range from 0.01 Hz to 100 kHz using an AC signal, a frequency response analyzer was used. Immersion tests were conducted to observe the priority substructure where corrosion occurs. The SCC susceptibility was evaluated using a slow speed tensile testing machine (MINOS-02 L, MTDI, Korea) under a strain rate of 10^{-6} s^{-1} in 3.5% NaCl solution at room temperature. Slow strain

rate test (SSRT) was performed under an anode and cathode applied potentials of ±0.1 V versus corrosion potential (E_{corr}).

Multiple characterization techniques were used to analyze the substructures of the QM and TM specimens. The normal direction (ND) and transverse direction (TD) surfaces of hot-rolled specimens were polished and etched with a Nital solution to observe the substructures and their boundaries by optical microscopy (I-Scope 2001, Leica, Germany) and scanning electron microscopy (SEM, JSM-7610F, JEOL, Japan). SEM-based energy dispersive spectrometry (EDS) analysis was conducted to examine corrosion products. All specimens for electron backscattered diffraction (EBSD) measurements were prepared by electropolishing and chemical etching (Lectropol-5, Struers^{TM}) with a solution of acetic acid (90 vol%) and perchloric acid (10 vol%) at 30 V. All EBSD data were acquired using a step size of ~1 μm at 20 kV and post-processed using TSL OIM data collection software (TSL OIM Analysis 8). Five or more EBSD scans were obtained for each specimen condition. Thermodynamic calculations were performed using Thermo-Calc software and a TCFE11 database.

The TEM specimens were prepared by mechanically polishing thin foils to a thickness of >100 μm, followed by jet-polishing in TenuPol-5 (Struers^{TM}) using a solution of 90% CH_3COOH and 10% $HClO_4$. Conventional bright-field (BF) and high-resolution (HR) TEM images were obtained with a JEOL 2010F microscope equipped with an aberration corrector and operated at an accelerator voltage of 200 kV. The TEM analysis was conducted to investigate carbides and cementites at the lath boundary. A combined TKD and TEM analysis was performed at the same positions in TEM specimens to determine the misorientation angles of the targeted sub-boundaries shown in the TEM images. The TKD was conducted with OPTIMUS^{TM} TKD detector head (e-Flash^{HR}, ARGUS^{TM} electron detection system, Bruker, Germany) in a focused ion beam milling system (FIB, FEI Helios Nanolab 650*i*). The TKD results were interpreted using Bruker EBSD software [55].

The APT needles were prepared using FIB on LAGB- and HAGB-containing regions detected during the lift-out procedure. The chemical compositions of alloying elements containing carbon and boron at the boundaries were investigated using an APT system (LEAP 4000X HR, Cameca Inc.). All measurements were performed in the voltage-pulsing mode. The detection rate, pulse fraction, and pulse repetition rate were 0.2%, 15%, and 200 kHz, respectively. All measurements were performed at 60 K at > 10^{-11} Torr. A commercial IVAS® software (ver. 3.8.4) by Cameca was employed following a previously reported protocol [56] to visualize the tomographic reconstruction.

3. Results

3.1. Crystallographic features

We classified the complex substructures of one martensite grain, i.e., lath, block, and packet, and PAGBs via EBSD (Supplementary Information Fig. S1). A martensite grain comprised several packets with different orientations and substructures of blocks and laths. According to the typical Kurdjumov–Sachs orientation relationship (KS OR), the misorientation angles (θ) below 10.53° were categorized as lath boundary, misorientation angles of 10.53° < θ < 51.73° were classified as PAGB or packet boundary, and the misorientation angles above 51.73° were denoted as block boundaries.

The EBSD inverse pole figure map (top panel) and image quality (IQ) plus boundary map (bottom panel) of QM and TM specimens are displayed in Fig. 1(a)–(d). The misorientation profiles in Fig. 1(e) and (f) reveal that the fractions of identified PAGBs and packet boundaries are low compared to those of lath and block boundaries for both specimens. This observation confirms that block boundaries with high misorientation angles can be treated as effective grain boundaries, which promote dislocation pile-up during deformation. Between the two steels, QM contained more lath boundaries with θ < 10.53° than TM, whereas TM had more block boundaries with θ > 51.73° The disappearance of laths occurring concurrent with the increase in blocks is the effect of the applied tempering on the substructures in the current martensite alloy.

With the aim of resolving a longstanding issue as to how these substructures in martensitic steels are discerned in any TEM-equipped laboratory, we conducted a correlative analysis using TEM and TKD on the TM specimen to determine the exact θ values of block and lath boundaries. Fig. 2(a) shows the TEM image of general martensite steel; the complex substructures with narrow widths, and profuse imaging fringes can be seen. All TEM-observed regions were successfully scanned via TKD measurements using the same TEM specimens. The TEM results cross-correlated with the θ measured by TKD are shown in Fig. 2(b)–(d), where the block and packet boundaries are marked in red and the subblock boundaries in blue to improve visibility. The lath boundaries (unmarked) were the most abundant in the TKD map. Local misorientation angle profiles were analyzed in a single former austenite grain across the lath boundaries. The misorientation angle profiling in Fig. 2(e) was performed at one PAGB to distinguish the boundary characteristics of the substructure. The misorientation angle of lath boundaries ranged from 1.0° to 3.0° and was distinguished from the other minor substructures with misorientation angles below 1.0° Sandvik and Waymann [57] confirmed via time-consuming electron diffraction pattern analysis that the orientation relationship between the KS OR ranges from 2.1° to 5.1° This study obtained similar results (0.5°–5.1°) by simply combining the TEM–TKD images.

Table 2
Tensile test results of QM and TM specimens.

Specimen	Yield strength (MPa)	Tensile strength (MPa)	Elongation (%)	Strain hardening exponent
QM	1380	1932	9.2	0.11
TM	1341	1704	12.5	0.09

3.2. Tensile properties

The tensile properties of the QM and TM specimens are shown in Fig. 3, and the corresponding property values are summarized in Table 2. Both specimens exhibited the same yield strength of 1.3 GPa. The QM exhibited higher tensile strength (1.9 GPa) than that of TM (1.7 GPa) owing to the higher strain hardening ratio and strain hardening exponent of QM (0.11) compared to that of TM (0.09). The tensile elongation of both specimens exceeded 9% owing to post-necking elongation after tensile strength. Both tensile-tested specimens showed the ductile fracture surfaces with delamination that increased the non-uniform elongation region after necking due to the bifurcation effect [58–60].

3.3. Corrosion properties

Fig. 4 shows the OCP curves, polarization curves, and impedance spectroscopy results of QM and TM specimens tested in 3.5% NaCl solution. The average OCP values of the martensitic steel in Fig. 4(a), measured at the stabilization stage, are −0.578 and −0.664 V_{SCE} for QM and TM specimens, respectively. Fig. 4(b) shows the potentiodynamic polarization curves for the TM and QM specimens. Here, E_{corr} is the boundary equilibrium potential between corrosion and anticorrosion and i_{corr} is the current density at the initial moment of corrosion measured by the Tafel method [61]. The procedure for obtaining the current density by the Tafel extrapolation method is shown in the enlarged view of the dotted

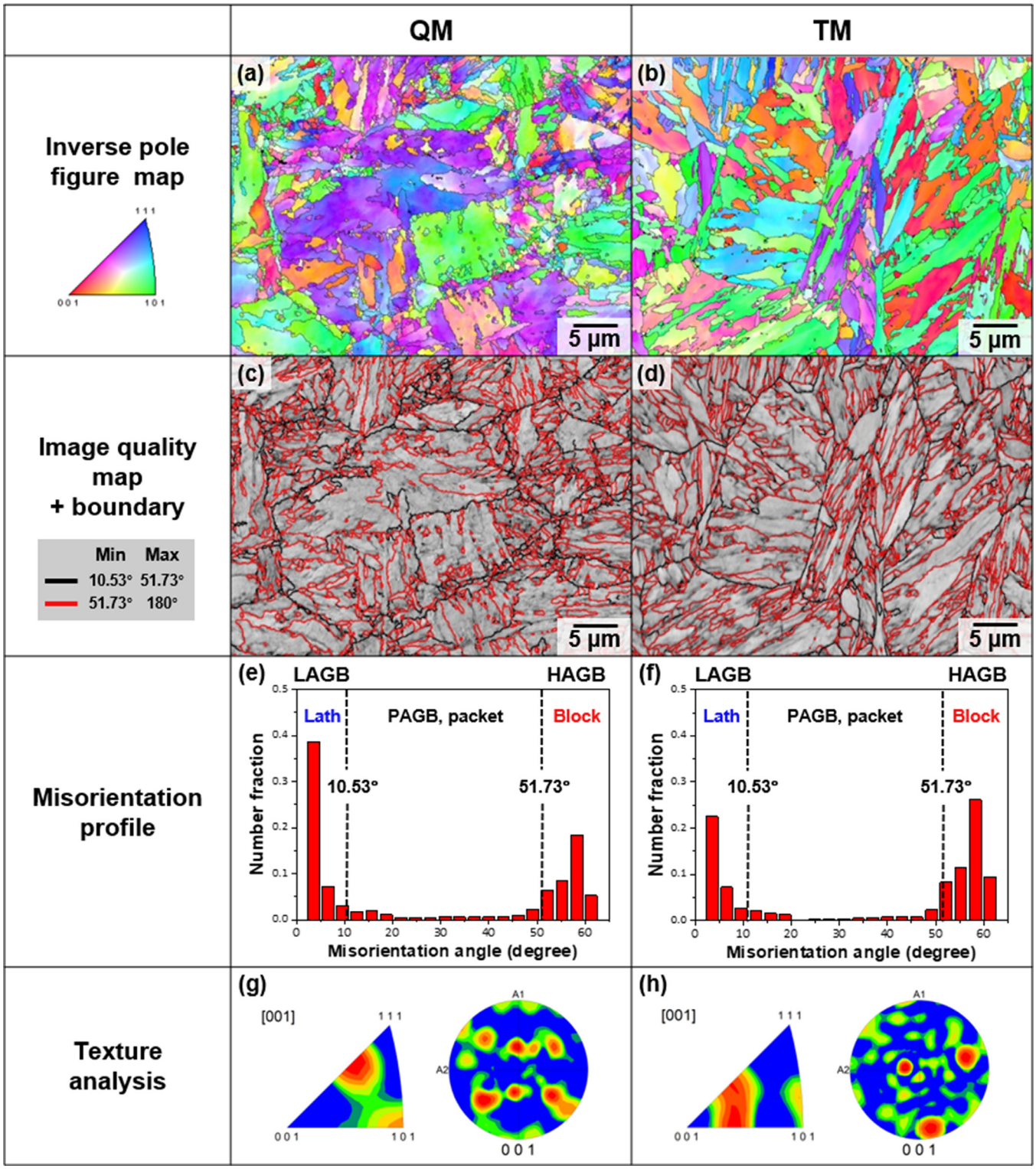

Fig. 1. Typical orientation imaging maps obtained from the EBSD measurement of the QM and TM specimens. (a, b) IPF map and (c, d) IQ map. According to KS OR, the black line in the range of 10.53° to 51.73° was PAGB, and the red line in the range of 51.73° to 180° was classified as block. (e, f) Misorientation profile results and (g, h) texture analysis of QM and TM specimens.

line box in Fig. 4(b). A high E_{corr} value indicates high resistance to corrosive attack, while low i_{corr} corresponds to slow corrosion speed. The E_{corr} values of QM and TM were –0.581 and –0.671 V_{SCE}, respectively, and the i_{corr} values were 2.91×10^{-6} and 2.76×10^{-6} A·cm^{-2}, respectively. For the reproducibility of the measurements, three potentiodynamic polarization curves for each specimen are provided in Supplementary Information Fig. S2. This result is unprecedented, as it contradicts the common knowledge that the tempering process enhances the polarization potential of martensitic steels [62,63]. The QM specimen (before tempering) exhibits higher corrosion resistance than the TM (after tempering). Therefore, the corrosion process will begin at lower E_{corr} values in TM

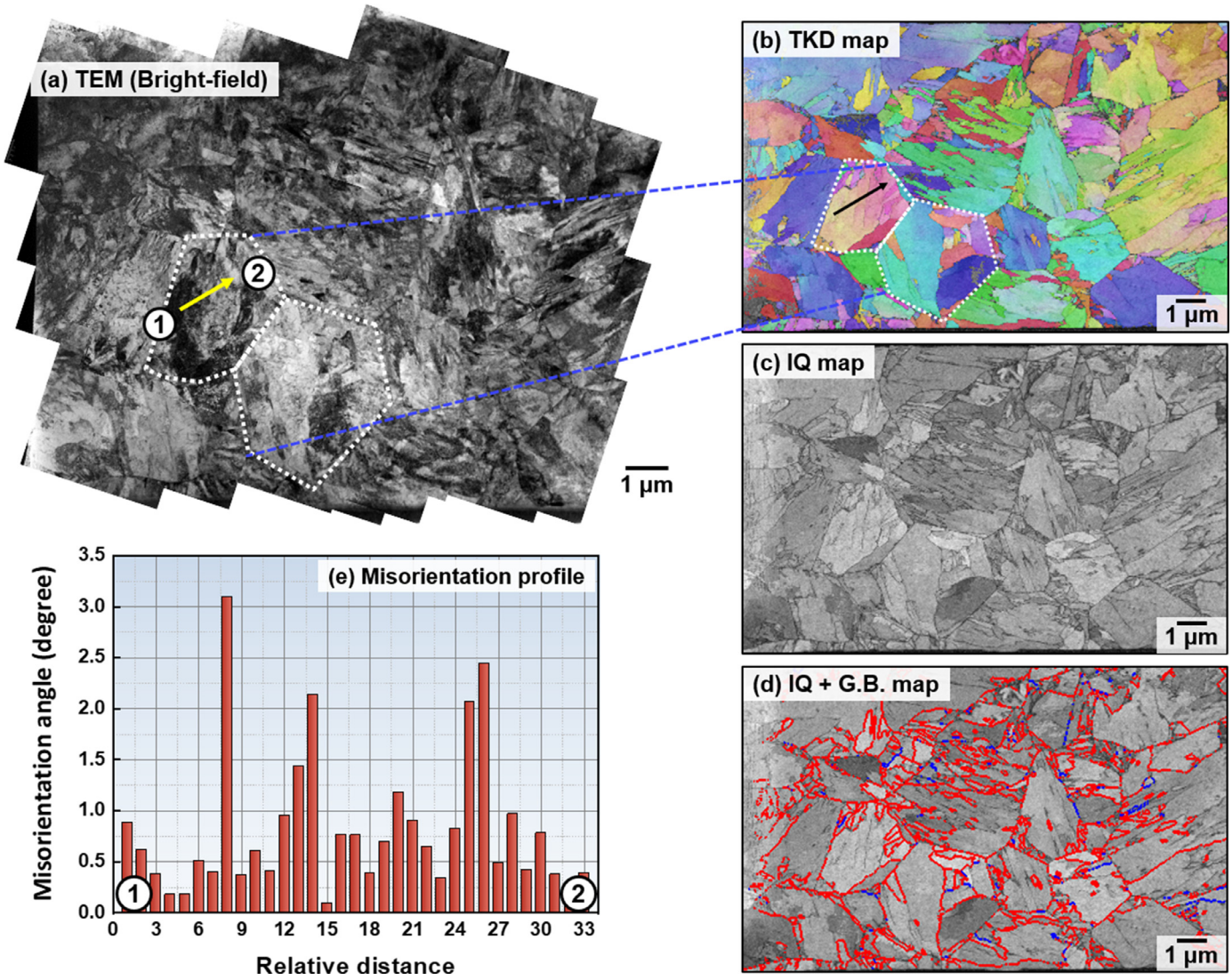

Fig. 2. Transmission Kikuchi diffraction (TKD) map matched with (a) TEM bright field image. (b) TKD map, (c) IQ map, and (d) IQ with grain boundary map. The block and packet boundaries are marked in red, and the sub-block boundaries are marked in blue for visibility. (e) Misorientation profile results from ① to ② inside the grain of (a) TEM bright field image.

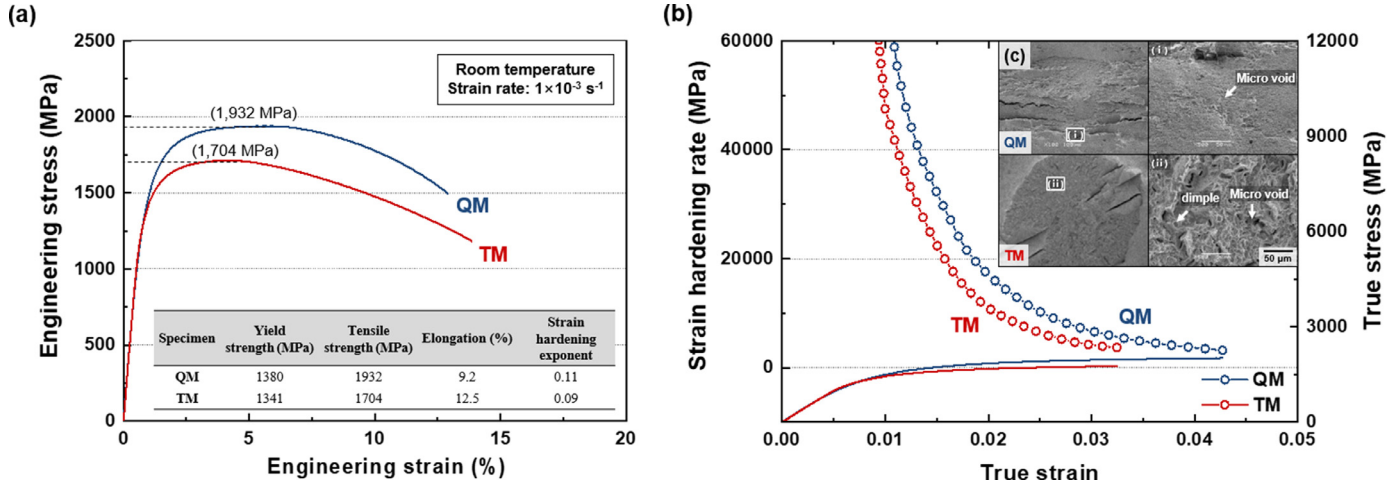

Fig. 3. (a) Engineering stress–strain curves of QM and TM specimens tensile tested at room temperature at a strain rate of 1×10^{-3} s^{-1}; yield strength, ultimate tensile strength, elongation, and strain hardening exponent are represented. (b) True stress–strain curves and strain hardening rate versus true strain for QM and TM specimens. (c) Fractography of QM and TM specimens at low magnification (left). (i) QM specimen and (ii) TM specimen image observed at high magnification (right).

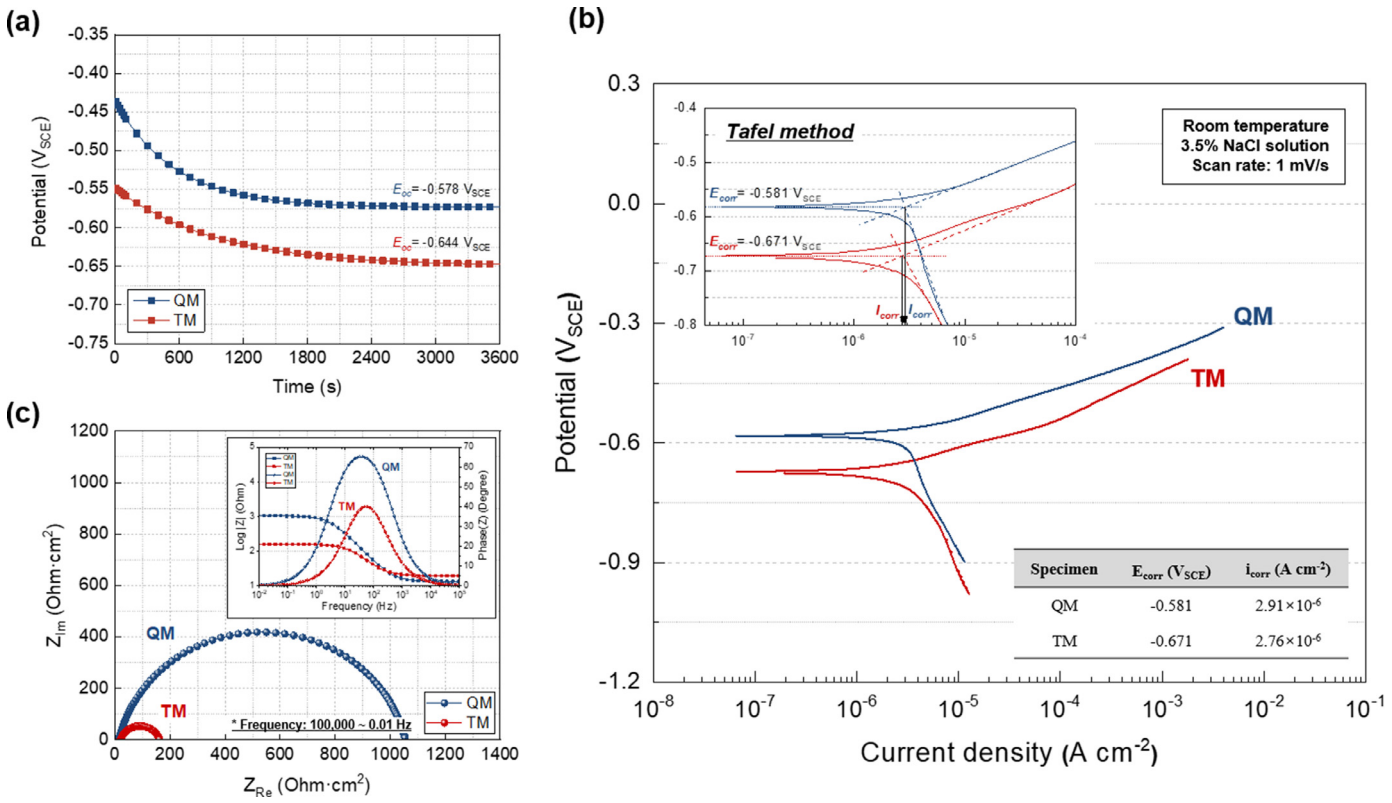

Fig. 4. (a) Time dependence of open circuit potential (OCP) graph evaluated for 3600 s in 3.5% NaCl solution. (b) Potentiodynamic polarization tests of QM and TM specimens in 3.5% NaCl solution with a scan rate of 1 mV/s; corrosion potential (E_{corr}) and current density (i_{corr}) are represented. Tests were performed at least three times for reliability. (c) Electrochemical impedance spectroscopy (EIS) test results using the Nyquist and Bode impedance plots. The frequency for EIS tests ranged from an initial 100,000 Hz to final 0.01 Hz with an amplitude of the sinusoidal potential signal of 10 mV with respect to OCP of QM and TM specimens in 3.5% NaCl solution.

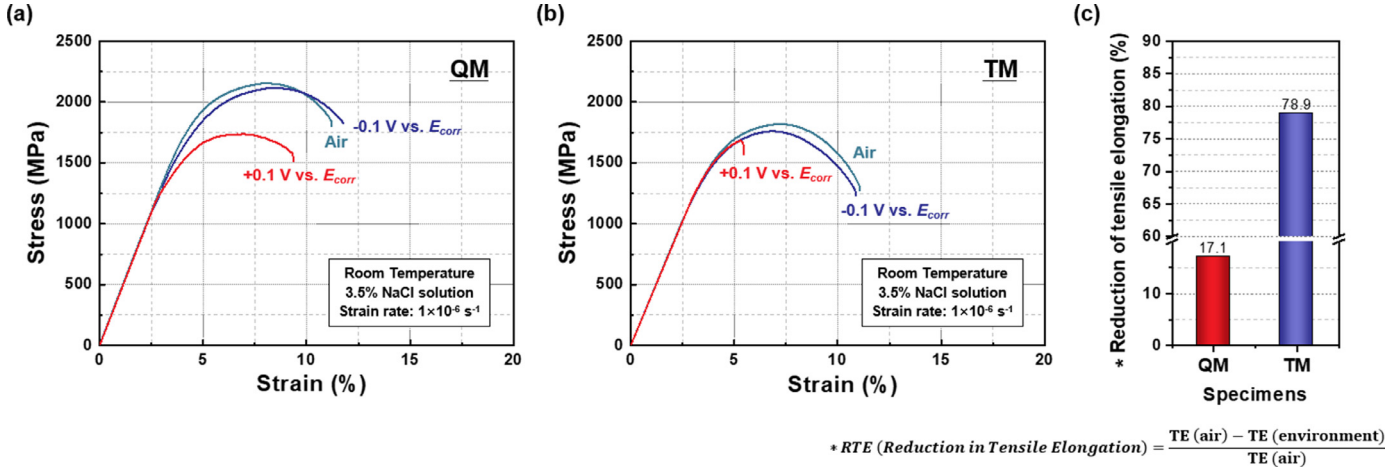

Fig. 5. The representative stress–strain curves of (a) QM and (b) TM specimens after SSRT at a strain rate of 1×10^{-6} s^{-1} in air and 3.5% NaCl solution at applied potentials of ±0.1 V vs. E_{corr}. The gradual slope of the elastic area is due to the difficulty of mounting the extensometer in environmental conditions. (c) The result of the reduction of tensile elongation (RTE) value of the QM and TM specimens.

despite its slower corrosion rate. Fig. 4(c) shows the Nyquist and Bode plots of both specimens obtained using EIS measurement in 3.5 wt.% NaCl solution under the OCP condition. The large diameter of the Nyquist semicircle, high absolute impedance |Z| at the lowest frequency, and high maximum phase angle (θ) of QM indicate its excellent corrosion resistance compared to that of TM.

3.4. SCC properties

The SSRT under E_{corr} ± 0.1 V (obtained from Fig. 4) is summarized in Fig. 5 and Table 3. The elongation of either specimen was not reduced by hydrogen embrittlement at –0.1 V vs. E_{corr}. Under the anodic condition (+0.1 V vs. E_{corr}), QM exhibited a reduced strength and elongation ratio, while TM had a decreased elongation ratio. The SCC corrosion resistance can be evaluated by the reduction of tensile elongation (RTE) [64,65]. The equation for RTE in 3.5% NaCl solution is

$$RTE\ (reduction\ in\ tensile\ elongation) = \frac{TE_{air} - TE_{3.5\%\ NaCl}}{TE_{air}} \times 100 \quad (1)$$

Table 3
SSRT results in air and 3.5% NaCl solution at applied potentials of ±0.1 V vs. E_{corr} in QM and TM specimens.

Specimen	Condition	Yield strength (MPa)	Tensile strength (MPa)	Tensile elongation (%)	Reduction of tensile elongation (%)
QM	In air	1753	2161	7.0	–
	−0.1 V vs. E_{corr}	1607	2119	7.4	0
	+0.1 V vs. E_{corr}	1269	1596	5.8	17.1
TM	In air	1418	1819	7.1	–
	−0.1 V vs. E_{corr}	1473	1760	7.2	0
	+0.1 V vs. E_{corr}	1315	1681	1.5	78.9

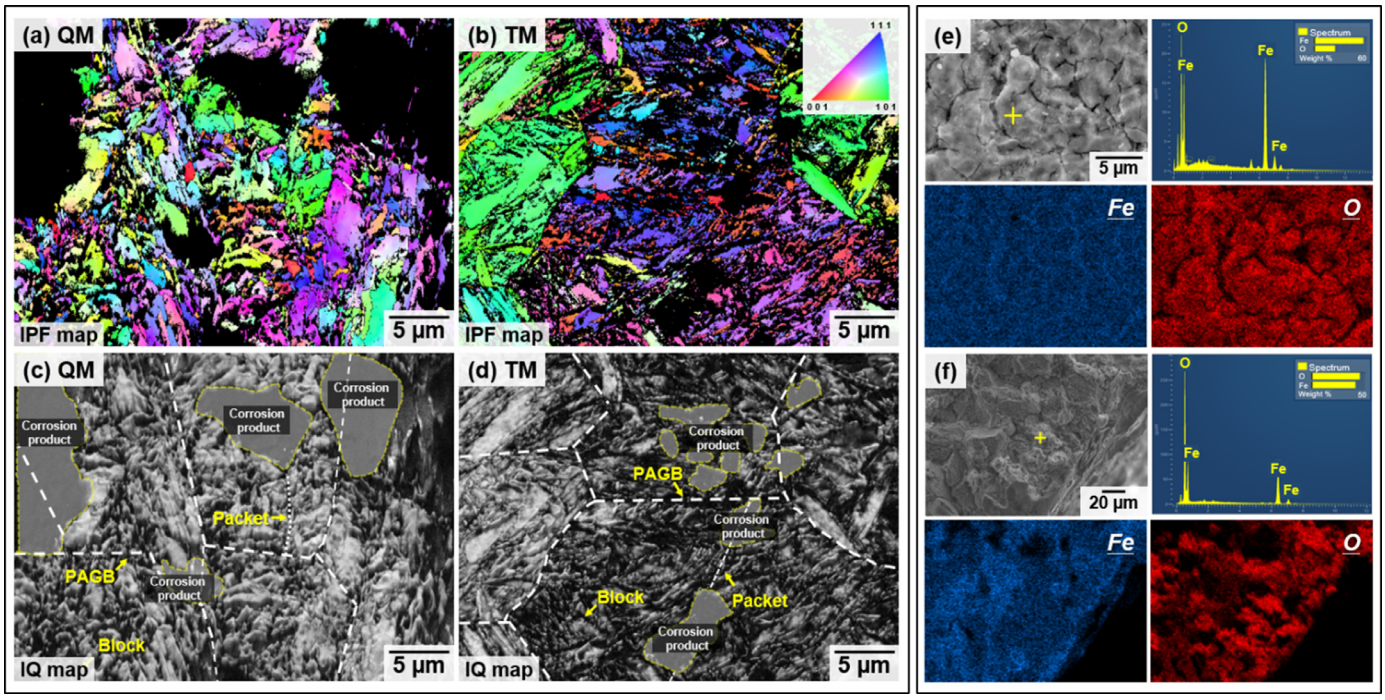

Fig. 6. (a, b) The inverse pole figure (IPF) map and (c, d) image quality (IQ) map analysis after immersion tests for 1 hour in 3.5% NaCl solution. In the IQ map, the block boundary and PAGB are indicated by white lines, and corrosion products are indicated by yellow lines. SEM–EDS results for corrosion product analysis after (e) the immersion test and (f) slow strain rate test (SSRT) for the QM specimen.

where TE_{air} is tensile elongation in air and $TE_{3.5\%\ NaCl}$ is tensile elongation in 3.5% NaCl solution condition. The RTE percentages of QM and TM were 17.1% and 78.9%, respectively, implying that QM had higher SCC resistance than TM.

4. Discussion

4.1. Microstructural factors influencing SCC

Corrosion products are examined by EBSD and EDS analysis after immersion test and SSRT as shown in Fig. 6. Black-colored zones with a low confidence index in the IPF map were confirmed to be corrosion products in the IQ map that were produced due to the formation of highly oxidized surfaces during corrosion tests. The size and location of the corrosive products were dependent on the applied tempering. The sizes of corrosive products for the QM and TM were estimated to be 5–10 and 2–3 μm, respectively. Most corrosive products in both specimens were located close to PAGB and packet boundaries, whereas corrosive products in the TM were found inside the grains. Fig. S4 shows the schematic diagram of the corrosive anodic and cathodic reaction in 3.5% NaCl solution. Corrosion products such as Fe_2O_3, Fe_3O_4, and $FeCO_3$ are formed by environmental effect. The EDS analysis (Figs. 6(e, f)) for the corrosion products confirms the presence of the aforementioned iron oxides after the immersion tests and SSRT.

We examined the possible carbides and cementite (Fe_3C) on subboundaries to determine the origin of the corrosive products. Based on the equilibrium phase diagram of the current alloy composition, cementite (Fe_3C) started to form at 690 °C above the ferrite single-phase region due to the reverse Gibbs free energies of ferrite and cementite (Supplementary Information Fig. S5). The single austenite phase was stable above 770 °C, and the dual-phase range of ferrite and austenite was 690–770 °C. Fine cementites preexisted before tempering in the QM specimen, and the volume fraction of cementites/carbides drastically increased during tempering. Multiple-scale characterizations were performed via EBSD, electron channeling contrast imaging (ECCI), and TEM for the carbides on the lath boundaries with θ values $< 10.53°$ Fig. 7(a)–(d) show the EBSD and cross-correlated ECCI images for the fine carbides formed on the lath boundaries for the TM specimen. Although these carbides are extremely small, they are assumed to be generally known as MC, M_7C_3, and $M_{23}C_6$ along the lath boundaries (M = Fe, Mn, Cr, Ti, or Mo), as confirmed by TEM observation. The TEM dark-field (DF) imaging and corresponding TEM-EDS maps of alloying elements, obtained using carbide extraction replica method, revealed the formation of $M_{23}C_6$-type sphere $(FeMnCr)_{23}C_6$ and MX-type cuboidal $(TiMo)_x(CN)_{1-x}$

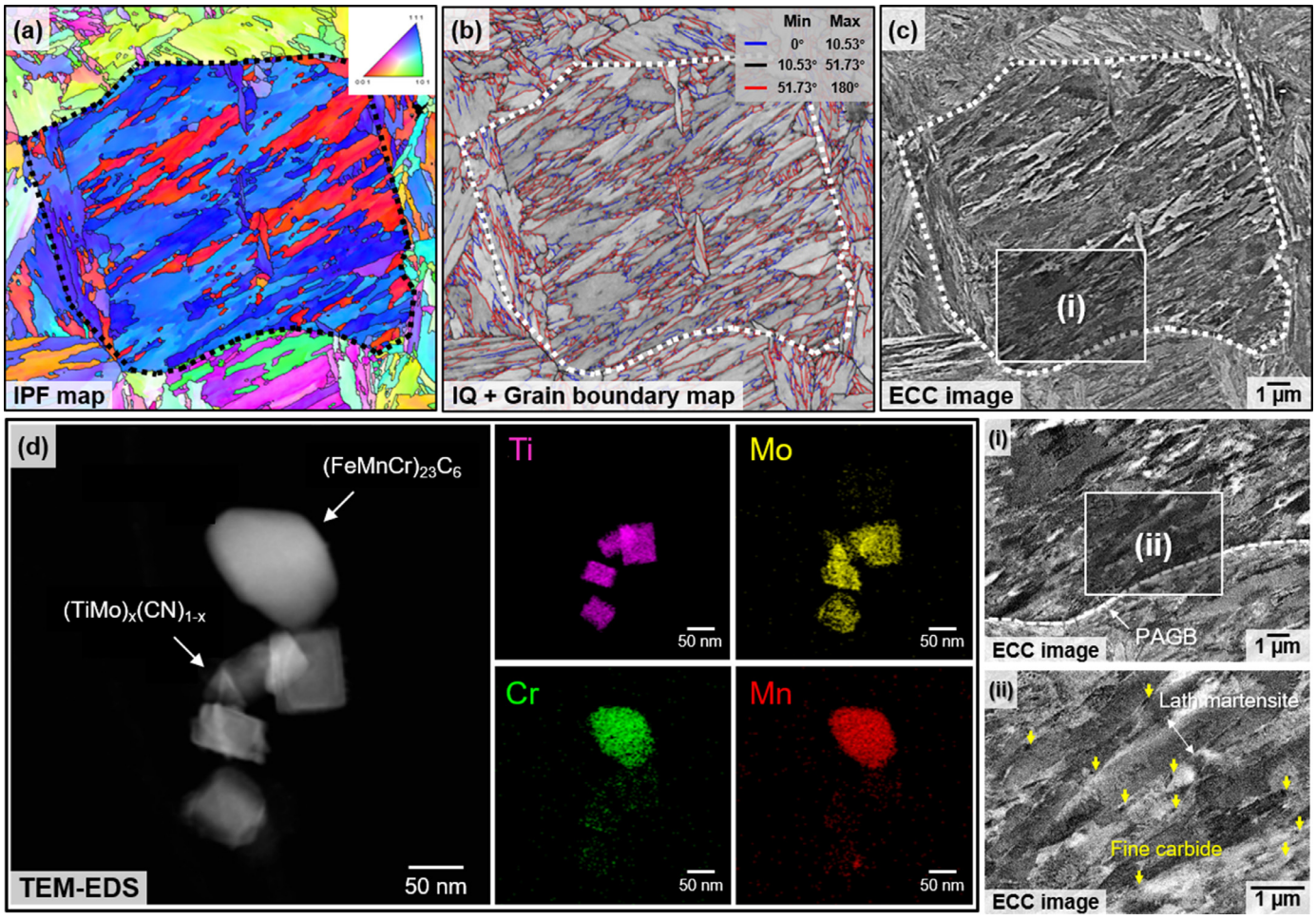

Fig. 7. (a) IPF map, (b) IQ map, and (c) ECCI of the TM specimen. The characteristics of grain boundaries in IQ map were categorized by KS OR. (i) and (ii) fine carbide on the lath boundary of martensite in (c). (d) TEM-EDS of spherical $(FeMnCr)_{23}C_6$ and angular $(TiMo)_x(CN)_{1-x}$ at the lath boundaries.

carbides (Fig. 7(e)). Based on our observations and literature, it is highly plausible that these carbides initially formed and grew at the lath boundaries during tempering.

The fracture surface and cross-sectional microstructure analysis of QM and TM after SSRT are shown in Fig. 8. As seen in Fig. 8(a, b), semi-cleavage fracturing with fine cracks from the surface to the center of the specimen occurred. Delamination and secondary cracking were observed with a dimple at the center of both specimens with intergranular fractures at the surface. The EBSD of the QM and TM cross-sections after SSRT is shown in Fig. 8(c, d) to analyze the boundary effect under stress and corrosion environments. In the QM specimen, stress corrosion cracks formed along PAGB, where more corrosion occurred compared to the other sub-boundaries. The cracking behavior of the TM specimen showed a network structure along the lath boundary that reduced strength and elongation. Therefore, in stress-induced and corrosive environments, PAGB is the preferential corrosion area in QM specimen, whereas the lath boundary is the mainly corroded region in the TM specimen.

4.2. Crystallographic orientation relationship

As summarized in Table 4, the crystallographic system has 24 equivalent variants satisfying KS OR, and the misorientation angles are categorized into 10 groups. Due to the transformation from austenite to martensite, packet boundaries of martensite should follow KS OR. Kitahara et al. [22] suggested that packet boundaries are in the range between 10.53° and 51.73°, lath boundaries are below 10.53°, and block or prior austenite grain boundaries are above 51.73° Fig. 1 shows the EBSD classification of sub-structure in the QM and TM specimens. The misorientation profiles of the QM and TM specimens showed higher volume fractions of lath boundaries under 10.53° and block boundaries over 51.73° than those obtained in the midrange angles. “Medium angle grain boundaries,” such as packet boundaries or PAGBs, showed low number fractions due to their large domain size. The lath and block boundaries were well developed together in the TM specimen, while the number fraction of lath boundary was dominant in the QM specimen. Lath structures were well developed by the athermal shear transformation of the QM specimen, while atoms were rearranged during tempering. Minor atomic migration occurred during tempering, which yielded similarly textured microstructures in the QM and TM specimens.

The distance from the free surface influenced the variant selection of martensite transformation. The misorientation angle of 24 possible variants was determined as the angle between the free surface and shear transformation directions. The 24 variants were not formed simultaneously during the martensitic transformation; some were transformed into subblocks with minor misorientation angles. The combination of two variants act as a block, and single variants are considered subblocks. Variant selection was decided to reduce the strain energy during lath formation. Among the close

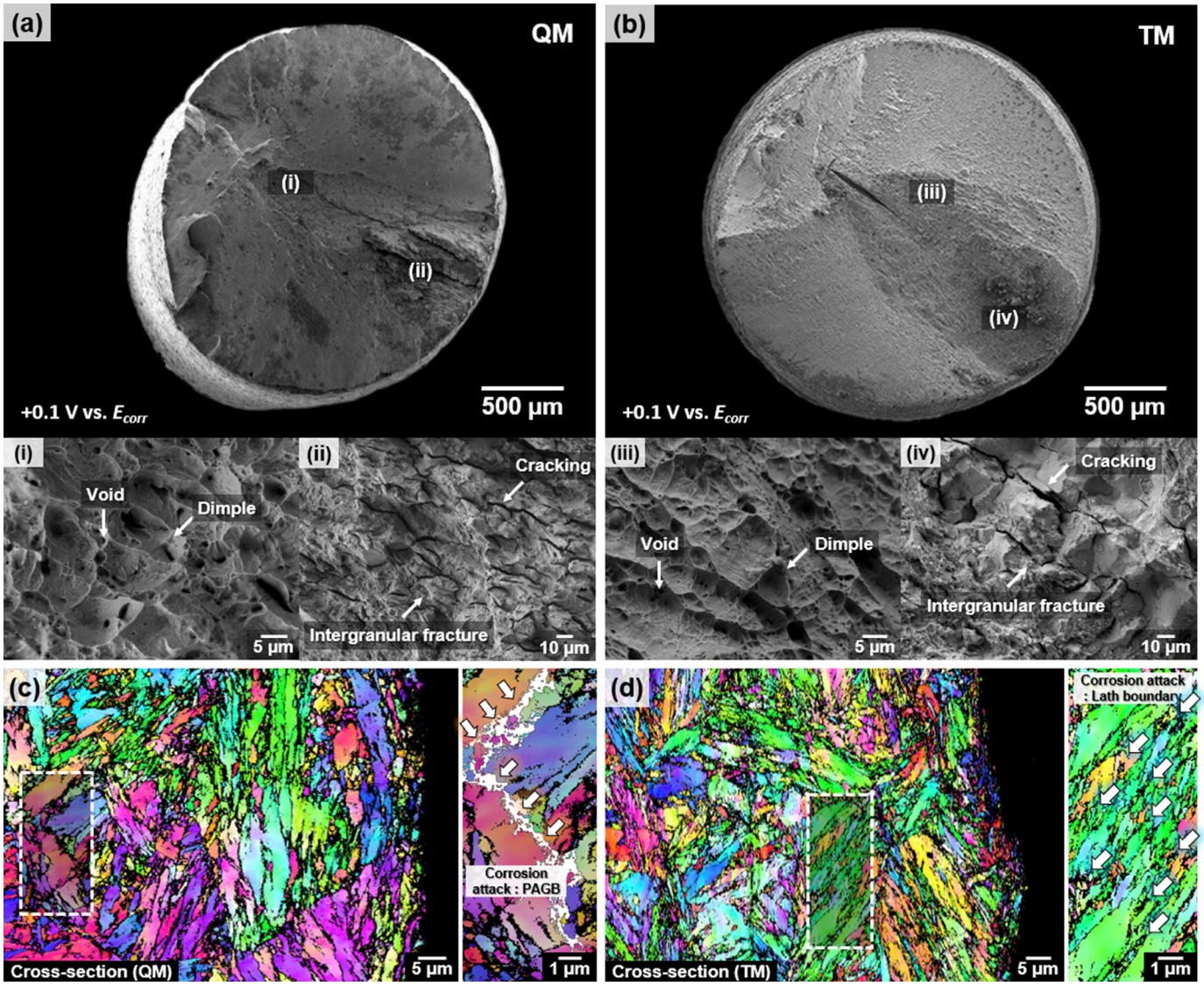

Fig. 8. Fractography of QM and TM specimens after SSRT in 3.5% NaCl solution at an anodic potential (+0.1 V vs. E_{corr}). Low magnification fractography of (a) QM and (b) TM specimens. (i) and (iii) void and dimple formation. (ii) and (iv) intergranular fracture and cracking. Cross-sectional EBSD analysis shows intergranular cracking of the (c) QM and (d) TM specimens after SSRT.

packed (CP) groups (CP1, CP2, CP3, and CP4), the variants most parallel to the free surface, such as a grain boundary or twin boundary, were selected first despite their small differences in misorientations. Subsequent variant selections for the remaining CP groups followed an increasing angle to the free surface.

Fig. 9 shows the texture analysis of tempered martensite before and after SSRT. The KS OR can be categorized into four groups transformed from equivalent $\{111\}_\gamma$ planes of the parent austenite. Each group includes six variants parallel to $\{111\}_\gamma$ CP planes and 24 crystallographic variants. These four groups are packets, and the six variants are blocks. The hierarchical microstructure, which was subdivided from austenite grains, affected the strength of steel. Fig. 9(a) shows the KS OR and a clear texture for most variants. Before SSRT, all CP groups were dominant near the (001) plane, showing regular correlations. Fig. 9(b) shows the deviant pole figure analysis results compared to those before SSRT. The CP1 and CP2 groups were dominant near the (001) plane, while CP3 and CP4 groups were prevalent near the (111) plane with irregularly textured pole figures resulting from the crystallographic change due to external loading after SSRT.

4.3. Effect of dislocation density on SCC behavior

The EBSD scans were conducted on the QM and TM specimens before and after testing of the tensile properties to measure the geometrically necessary dislocations (GNDs). The EBSD kernel average misorientation (KAM) maps are shown in Supplementary Information Fig. S3. The GND values can be calculated as below [66]

$$\rho_{GND} = \frac{2\theta}{ub} \cdot (m^{-2}), \tag{2}$$

where θ is misorientation angle, u is the step size (0.1 μm), and b is the size of the Burgers vector (0.248 nm). The GND value of QM (2.12×10^{15} m^{-2}) was higher than that of TM (1.32×10^{15} m^{-2}) for the undeformed state, whereas the GND values of both tensile-tested specimens were nearly identical.

Dislocation hardening resulted from long-range ordered interactions following the Taylor strengthening equation,

$$\Delta\sigma_\rho = m\alpha Gb\rho^{0.5}, \tag{3}$$

Table 4
Crystal orientations of 24 martensite transformed from a (001) oriented austenite maintaining the KS OR, and crystallographic relationships between V1 and other variants.

Variant	Plane Parallel	Direction Parallel	Crystal orientations of martensite variants		Misorientation angle from V1 (°)	Misorientation axis between V1 and other variants	CSL
			(h k l)	[u v w]			
V1	$(111)_\gamma \parallel (011)_{\alpha'}$	$[\bar{1}01]_\gamma \parallel [\bar{1}\bar{1}1]_{\alpha'}$	(0.075 0.167 0.983)	[0.742 0.650 0.167]	–	–	–
V2		$[\bar{1}01]_\gamma \parallel [\bar{1}1\bar{1}]_{\alpha'}$	(0.650 0.167 0.742)	[0.167 0.983 0.074]	60.00	[0.577 0.577 0.577]	Σ3
V3		$[01\bar{1}]_\gamma \parallel [\bar{1}\bar{1}1]_{\alpha'}$	(0.742 0.167 0.650)	[0.667 0.075 0.742]	60.00	[0.000 0.707 0.707]	–
V4		$[01\bar{1}]_\gamma \parallel [\bar{1}1\bar{1}]_{\alpha'}$	(0.075 0.167 0.983)	[0.667 0.742 0.075]	10.53	[0.000 0.707 0.707]	Σ1
V5		$[1\bar{1}0]_\gamma \parallel [\bar{1}\bar{1}1]_{\alpha'}$	(0.667 0.075 0.742)	[0.075 0.983 0.167]	60.00	[0.000 0.707 0.707]	–
V6		$[1\bar{1}0]_\gamma \parallel [\bar{1}1\bar{1}]_{\alpha'}$	(0.667 0.075 0.742)	[0.742 0.167 0.650]	49.47	[0.000 0.707 0.707]	Σ11
V7	$(1\bar{1}1)_\gamma \parallel (011)_{\alpha'}$	$[10\bar{1}]_\gamma \parallel [\bar{1}\bar{1}1]_{\alpha'}$	(0.167 0.650 0.742)	[0.983 0.167 0.075]	49.47	[0.577 0.577 0.577]	Σ19b
V8		$[10\bar{1}]_\gamma \parallel [\bar{1}1\bar{1}]_{\alpha'}$	(0.167 0.075 0.983)	[0.650 0.742 0.167]	10.53	[0.577 0.577 0.577]	Σ1
V9		$[\bar{1}\bar{1}0]_\gamma \parallel [\bar{1}\bar{1}1]_{\alpha'}$	(0.075 0.667 0.742)	[0.167 0.742 0.650]	50.51	[0.615 0.186 0.767]	–
V10		$[\bar{1}\bar{1}0]_\gamma \parallel [\bar{1}1\bar{1}]_{\alpha'}$	(0.075 0.742 0.667)	[0.983 0.167 0.075]	50.51	[0.739 0.462 0.490]	–
V11		$[011]_\gamma \parallel [\bar{1}\bar{1}1]_{\alpha'}$	(0.167 0.075 0.983)	[0.742 0.667 0.075]	14.88	[0.933 0.354 0.065]	Σ1
V12		$[011]_\gamma \parallel [\bar{1}1\bar{1}]_{\alpha'}$	(0.742 0.167 0.650)	[0.667 0.075 0.742]	57.21	[0.357 0.603 0.714]	–
V13	$(\bar{1}11)_\gamma \parallel (011)_{\alpha'}$	$[0\bar{1}1]_\gamma \parallel [\bar{1}\bar{1}1]_{\alpha'}$	(0.167 0.075 0.983)	[0.742 0.667 0.075]	14.88	[0.354 0.933 0.065]	Σ1
V14		$[0\bar{1}1]_\gamma \parallel [\bar{1}1\bar{1}]_{\alpha'}$	(0.167 0.650 0.742)	[0.075 0.742 0.667]	50.51	[0.490 0.462 0.739]	–
V15		$[\bar{1}0\bar{1}]_\gamma \parallel [\bar{1}\bar{1}1]_{\alpha'}$	(0.167 0.742 0.650)	[0.983 0.075 0.167]	57.21	[0.738 0.246 0.628]	–
V16		$[\bar{1}0\bar{1}]_\gamma \parallel [\bar{1}1\bar{1}]_{\alpha'}$	(0.167 0.075 0.983)	[0.650 0.742 0.167]	20.61	[0.659 0.659 0.363]	–
V17		$[110]_\gamma \parallel [\bar{1}\bar{1}1]_{\alpha'}$	(0.075 0.742 0.667)	[0.167 0.650 0.742]	51.73	[0.659 0.363 0.659]	–
V18		$[110]_\gamma \parallel [\bar{1}1\bar{1}]_{\alpha'}$	(0.075 0.667 0.742)	[0.983 0.075 0.167]	47.11	[0.719 0.302 0.626]	–
V19	$(11\bar{1})_\gamma \parallel (011)_{\alpha'}$	$[\bar{1}10]_\gamma \parallel [\bar{1}\bar{1}1]_{\alpha'}$	(0.742 0.075 0.667)	[0.650 0.167 0.742]	50.51	[0.186 0.767 0.615]	–
V20		$[\bar{1}10]_\gamma \parallel [\bar{1}1\bar{1}]_{\alpha'}$	(0.667 0.075 0.742)	[0.075 0.983 0.167]	57.21	[0.357 0.714 0.603]	–
V21		$[0\bar{1}\bar{1}]_\gamma \parallel [\bar{1}\bar{1}1]_{\alpha'}$	(0.075 0.167 0.983)	[0.667 0.742 0.075]	20.61	[0.955 0.000 0.296]	–
V22		$[0\bar{1}\bar{1}]_\gamma \parallel [\bar{1}1\bar{1}]_{\alpha'}$	(0.650 0.167 0.742)	[0.742 0.075 0.667]	47.11	[0.302 0.626 0.719]	–
V23		$[101]_\gamma \parallel [\bar{1}\bar{1}1]_{\alpha'}$	(0.650 0.167 0.742)	[0.167 0.983 0.075]	57.21	[0.246 0.628 0.738]	–
V24		$[101]_\gamma \parallel [\bar{1}1\bar{1}]_{\alpha'}$	(0.075 0.167 0.983)	[0.742 0.650 0.167]	21.06	[0.912 0.410 0.000]	–

where m is the average Taylor factor, α is a fitting parameter, G is the shear modulus, b is the Burgers vector, and ρ is the dislocation density. In bcc steel alloys, the Taylor factor is 2.75, the shear modulus is 78 GPa, and the Burgers vector for the <111> slip plane is 0.248 nm as stated above [67,68]. The value of α is 0.166, as derived from the linear regression method in low dislocation density alloy [69]. Strength contribution of the QM and TM specimens by dislocation hardening are calculated to be 400 and 320 MPa, respectively. Therefore, high total dislocation density aided to enhance the stress level of the QM specimen.

Morsdorf et al. [70] revealed that different dislocation densities in thin and coarse laths affect the strengthening of martensite. Preferentially formed laths become coarser due to auto-tempering, while subsequently formed laths have a thin morphology due to their low formation temperature above the martensite finish temperature. Coarse laths can achieve low dislocation densities earlier than thin laths, where low dislocation densities are achieved later in the phase transformation process. Compared to thin laths, coarse laths exhibit effectively enhanced ductility due to their low dislocation density aided by strain hardening [71].

Fig. 10 shows each thin and coarse lath in the TM specimen after SSRT to elucidate the combined effect of stress and environment. According to KAM and ECCI analysis (Fig. 10(e)), the average GND density of thin lath was higher (green) than that of the coarse lath (blue). Tangled dislocation cell structures were formed in the coarse lath, while the thin lath presented a high dislocation density, as denoted by the white ECC image. The thin laths increase the strength of the martensite with their high GND density, while coarse laths increase the ductility with their low GND density. The deformation is concentrated in the thin laths, leading to an increase in GND density. Meanwhile, corrosion attacks are localized in the high GND density area, and premature corrosion is expected to occur in the thin lath instead of the coarse lath. Despite their contribution to work hardening, thin laths are vulnerable to corrosion attack due to their high GND density. For this reason, it is difficult to surmount the strength–corrosion trade-off by controlling the morphology of microstructures.

4.4. Atomic segregation in the boundary

Fig. 11 shows the APT reconstruction of C atoms (cyan) and other alloying elements in the TM specimen. By choosing the isoconcentration surfaces (yellow) of ~0.9 at% carbon in the map, the lath boundary and PAGB were differentiated. Three zones, i.e., top, middle, and bottom grains, were divided clearly by the identified lath boundary and PAGB. The 2D density map from each grain shows the presence of poles identified as the crystallographic planes (110), (211), (222), and (121). The top and middle grains were in one prior austenite grain, while the bottom was in another. The top grain and middle grain, which were divided by a lath boundary, shared the same sequence of (110), (211), and (222) planes. The misorientation angle of the lath boundary was 8°, representing the LAGB, and that of the PAGB was 29°, representing the HAGB. The PAGB separated the middle and bottom grains, particularly by B and P co-segregation. The distribution of atomic elements (Mn, Ni, Mo, B, and P) is displayed in Fig. 11(b), and the composition profile was obtained across the grain boundary. The C atoms were aggregated at the lath boundary and PAGB, while B atoms were partitioned only at the PAGB.

According to APT analysis, numerous C atoms are densely localized at the lath boundary and PAGB (Fig. 12(a)). C atoms can diffuse through the lath boundary along the dislocation path, whereas their movement is blocked by PAGB. Compared to the lath boundary with its low energy, PAGB with high energy is thermodynamically favorable for atomic segregation. Thus, the dislocation path is prevalent in the lath. The segregation of C atoms is kinetically difficult to occur in fully martensitic steels due to insufficient diffusion time during quenching [72]. However, C diffusion occurs at a very rapid rate in martensitic steel; therefore, the atomic segregation of C atoms at grain boundary is difficult to disturb [73]. The segregation of C at grain boundaries is known to enhance the cohesion of grain boundaries [74]. Meanwhile, grain boundary cohesion decreases because of the segregation of harmful impurities (N, O, Si, P, S, or Mn), leading to intergranular embrittlement [75].

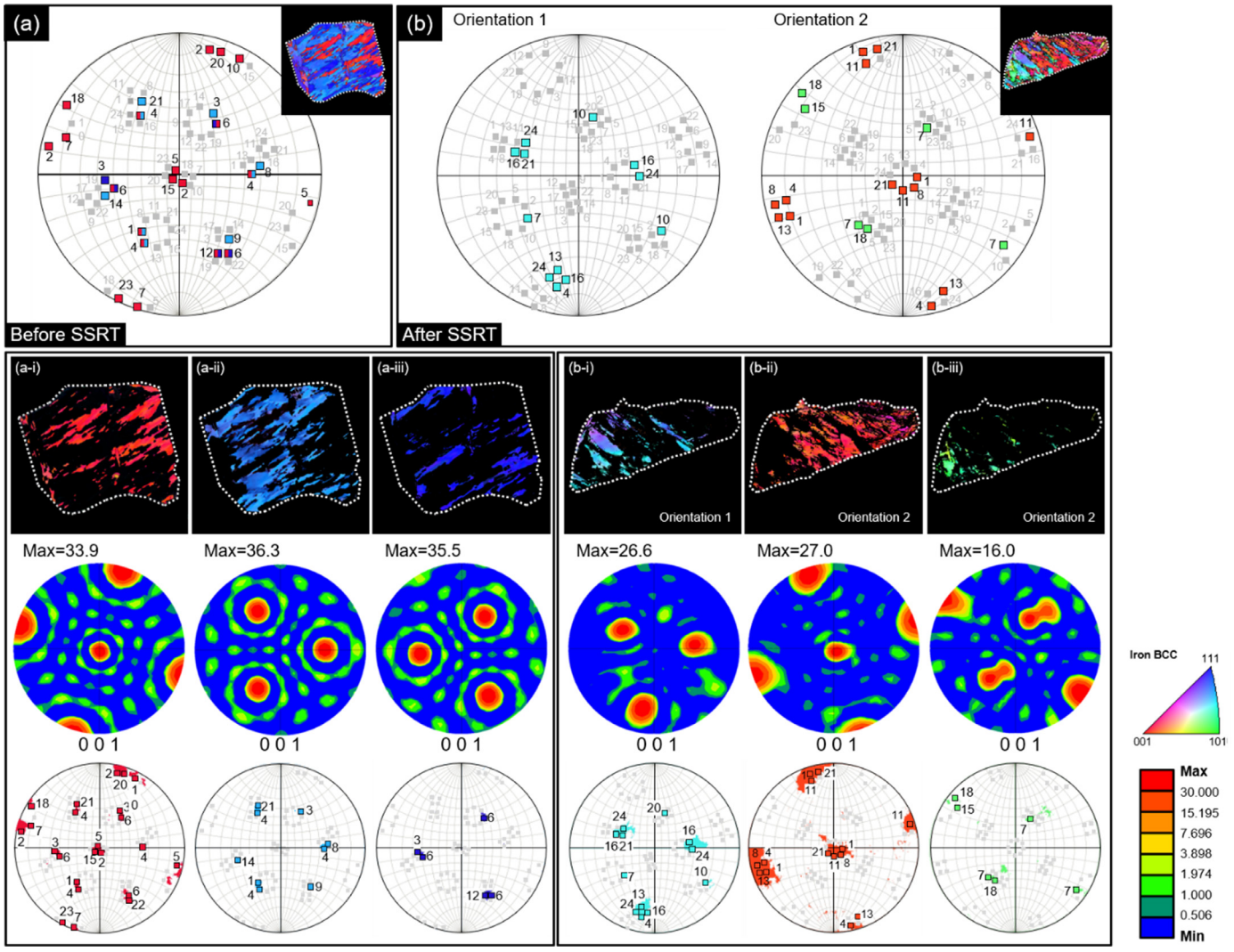

Fig. 9. {001} Pole figures denoting orientations of 24 martensite variants transformed from a single austenite grain maintaining the KS OR. Pole figure (PF) and IPF map of cross-sectional analysis (a) before and (b) after SSRT. (a-i), (a-ii), and (a-iii) the cropped images and PFs of (a) no deformed grain in TM specimen. (b-i), (b-ii), and (b-iii) the cropped images and PFs of the deformed grain in (b).

In particular, Mn can directly weaken the metallic bonds in the grain boundary by inducing structural relaxation [76,77], decreasing sublimation enthalpy [78], and attracting charges due to its low electronegativity [79]. These theories confirm that large Mn atoms lead to intergranular embrittlement, which is in agreement with the first-principle calculations [79–81]. According to the McLean equilibrium segregation theory, grain boundary segregation is closely proportional to the atomic density inside grains [82,83]. The distribution of Mn was homogeneous and proportional to Mn content. However, the theory cannot explain the segregation of B in grain boundaries.

The difference between equilibrium and non-equilibrium segregation is explained by two terms, namely, solute atoms and vacancy–solute atom complexes. Lejček et al. [84] suggested that non-equilibrium segregation is the interaction between solute atoms and the point defects induced by polycrystalline metals with grain boundaries. In non-equilibrium segregation, segregation width widens by back-diffusion during desegregation, and the concentration of B atoms at the PAGBs is higher than that in equilibrium segregation [85,86]. In Fig. 12(b, c), the chemical composition profile obtained across the PAGB confirms the dense segregation of B atoms at the PAGB.

The non-equilibrium segregation of B at the PAGBs decreases the grain boundary energy and reduces the diffusion of Mn to PAGBs. At elevated temperatures, equilibrium vacancy concentration increases, and complex short-range ordering between vacancy and B atoms form via attraction [87–89]. Vacancy and B clusters are carried to the PAGBs, reducing the vacancies in the inner grains. The migration of B atoms results in the formation of an enrichment area at the PAGBs. During tempering, B partially desegregates from the PAGB and migrates to martensite lath boundaries in conjunction with promoted segregation of Mn, causing an embrittling effect [72]. In this regard, B segregation at the PAGB could be encouraged to reduce the embrittlement of boundary owing to the pre-occupation of B atoms prior to other harmful elements.

The difference in segregation behavior between B and C can be explained by their different size, solubility, and diffusivity. The behavior of B atoms is significantly different from that of C atoms in steel. The atomic diameter of the B atom is too small (0.188 nm) to take up a substitutional position in iron (0.252 nm) and too large to occupy octahedral sites in austenite (0.109 nm) or in ferrite (0.038 nm). Calculations based on estimates of the atomic radius of B suggest that B may be substitutional in ferrite [85]. On

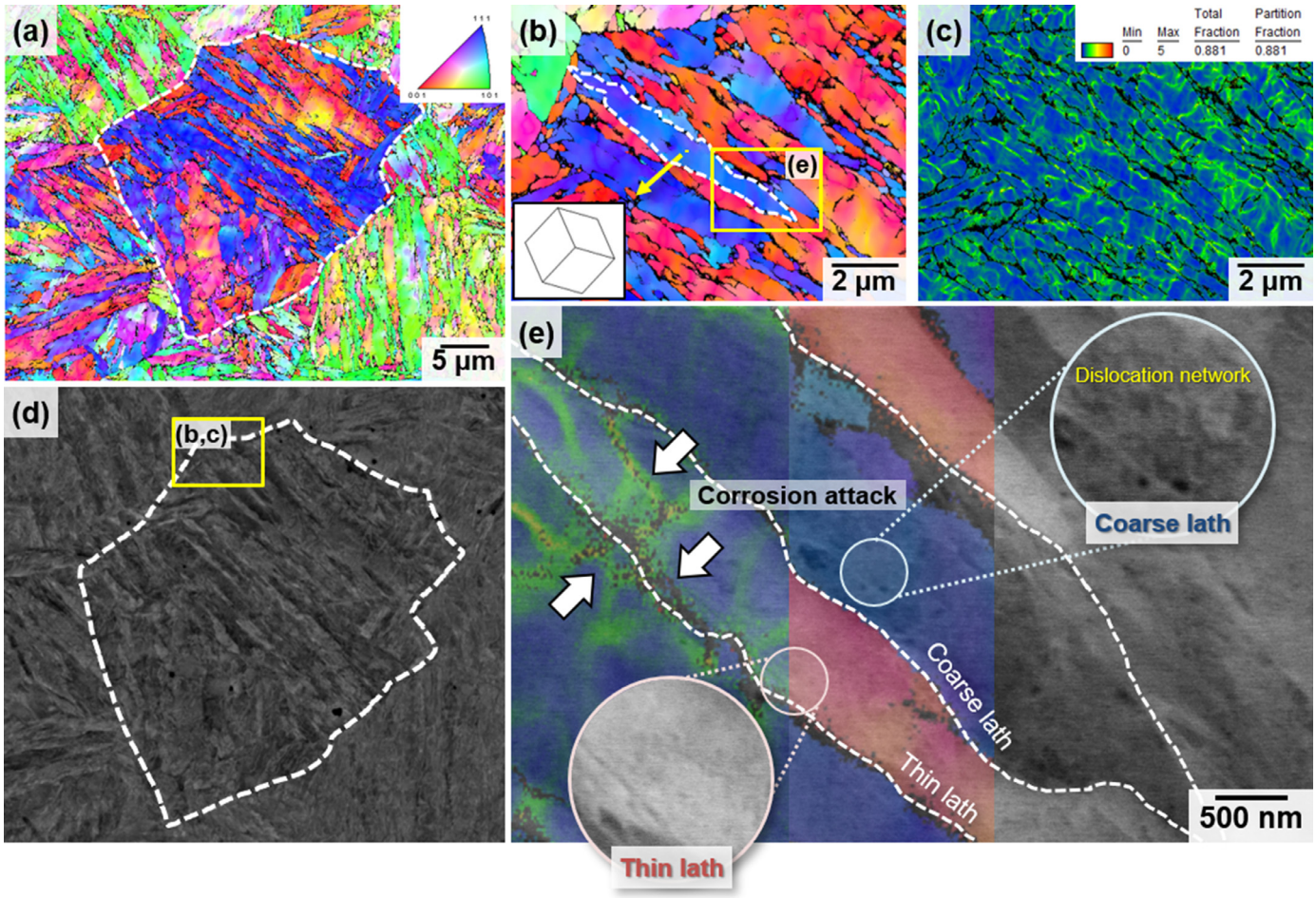

Fig. 10. Microstructure analysis of TM specimen after SSRT. (a) IPF map and (d) ECCI represent the same area of a prior austenite grain (PAG). (b) IPF map and (c) kernel average misorientation (KAM) map show high magnification of the yellow box in (d) ECCI. (e) KAM and IPF maps are overlapped in the ECCI showing high magnification of the yellow box in (b).

the other hand, the atomic diameter of C atoms (0.154 nm) is appropriate for largely dissolving in the interstitial sites of the iron lattice; this finding is consistent with the solubility of C atoms in iron. Therefore, the solubility of B is low in both austenite (0.02 wt% at 1149 °C) and ferrite (0.0004 wt% below 700 °C). By comparison, C atoms are more soluble than B atoms in both austenite (2.11 wt% at 1148 °C) and ferrite (0.0218 wt% at 727 °C). The equations for the diffusion coefficient of B [90,91] and C [92] are given as:

$$\textit{Boron diffusivity in ferrite}\left(m^2/s\right) : D_B = 2.0 \times 10^{-7} \exp\left(\frac{-27200}{RT}\right) \quad (4)$$

$$\textit{Carbon diffusivity in ferrite}\left(m^2/s\right) : D_C = 6.2 \times 10^{-7} \exp\left(\frac{-80000}{RT}\right) \quad (5)$$

According to Eqs. (4)–(5), the diffusion coefficient of B was higher than that of C due to low activation energy. It is deduced that B atoms readily occupy PAGB sites prior to C atoms. Therefore, we have gained an insight to the different segregation behavior of B atoms and C atoms by considering their size, solubility, and diffusivity factors.

4.5. Effect of cementites on SCC

Fine cementites resided at the lath boundaries and PAGBs, as confirmed by TEM BF, high-angle annular dark-field (HAADF), and diffraction pattern (DP) analysis (Fig. 13). Epitaxially grown lath microstructures were well developed in both QM and TM specimens. Measured lath widths were ~50 nm in both specimens. Cementite (Fe_3C) had the [122] zone axis, and martensite had the [012] and [113] zone axes in the QM and TM specimens, respectively. Mainly located at the lath boundaries, cementites precipitate and coarsen through tempering. Fine cementites were observed at the lath boundaries of the QM specimen in the HAADF image, and thickened cementite produced by tempering was mainly distributed at the lath boundary in the TM specimen. The width of cementites was larger in the TM specimen (27.3 ± 7.3 nm) than that in the QM specimen (16.0 ± 3.7 nm). The number of cementites per unit area was 3.32 and 15.38 ea/μm^2 in the QM and TM specimens, respectively. Cementites formed during tempering at the lath boundaries acted as SCC initiation sites. Therefore, the corrosion potential of the TM specimen is lower than that of the QM specimen, as shown in Fig. 4. The ε-Carbides, Fe_5C_2, and Fe_3C are formed at 100–250 °C, 250–350 °C, and 350–400 °C, respectively. [93,94] The number of cementites was counted during tempering at 180 °C. We found that cementites rarely formed during tempering, and the preexisting cementites coarsened. The coarsened cementites affected the SCC sensitivity of martensitic steel, result-

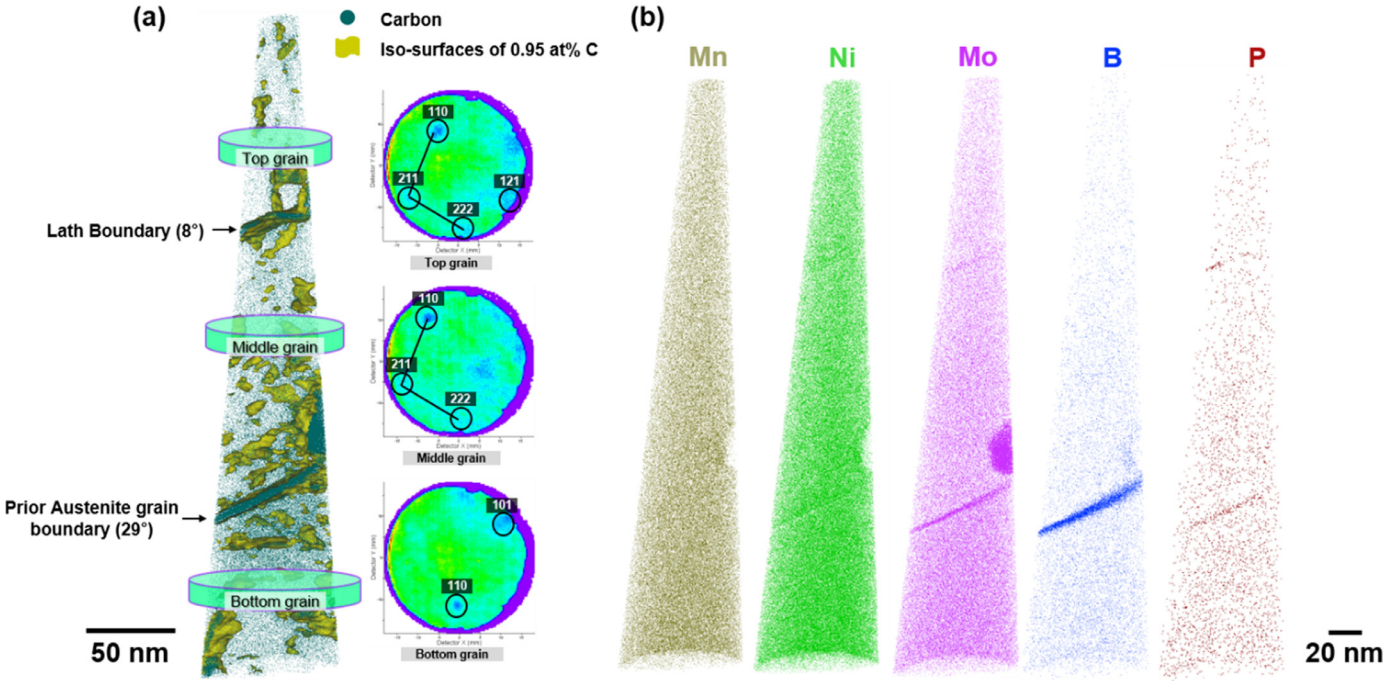

Fig. 11. 3D atomic probe reconstruction of a nanotip taken in the vicinity of the PAG and lath boundaries in the TM specimen. Green dots are C atoms, and the yellow area is the isosurface of 0.95% C. The needle-shaped specimen was divided into three groups: top, middle, and bottom grain. The lath boundary with misorientation angle of 8° and the PAGB with misorientation angle of 29° are in between each grain. The grain orientation is confirmed by cross-sectional 2D density mapping. The positioning of Mn, Ni, Mo, B, and P atoms are present in the APT tip reconstruction.

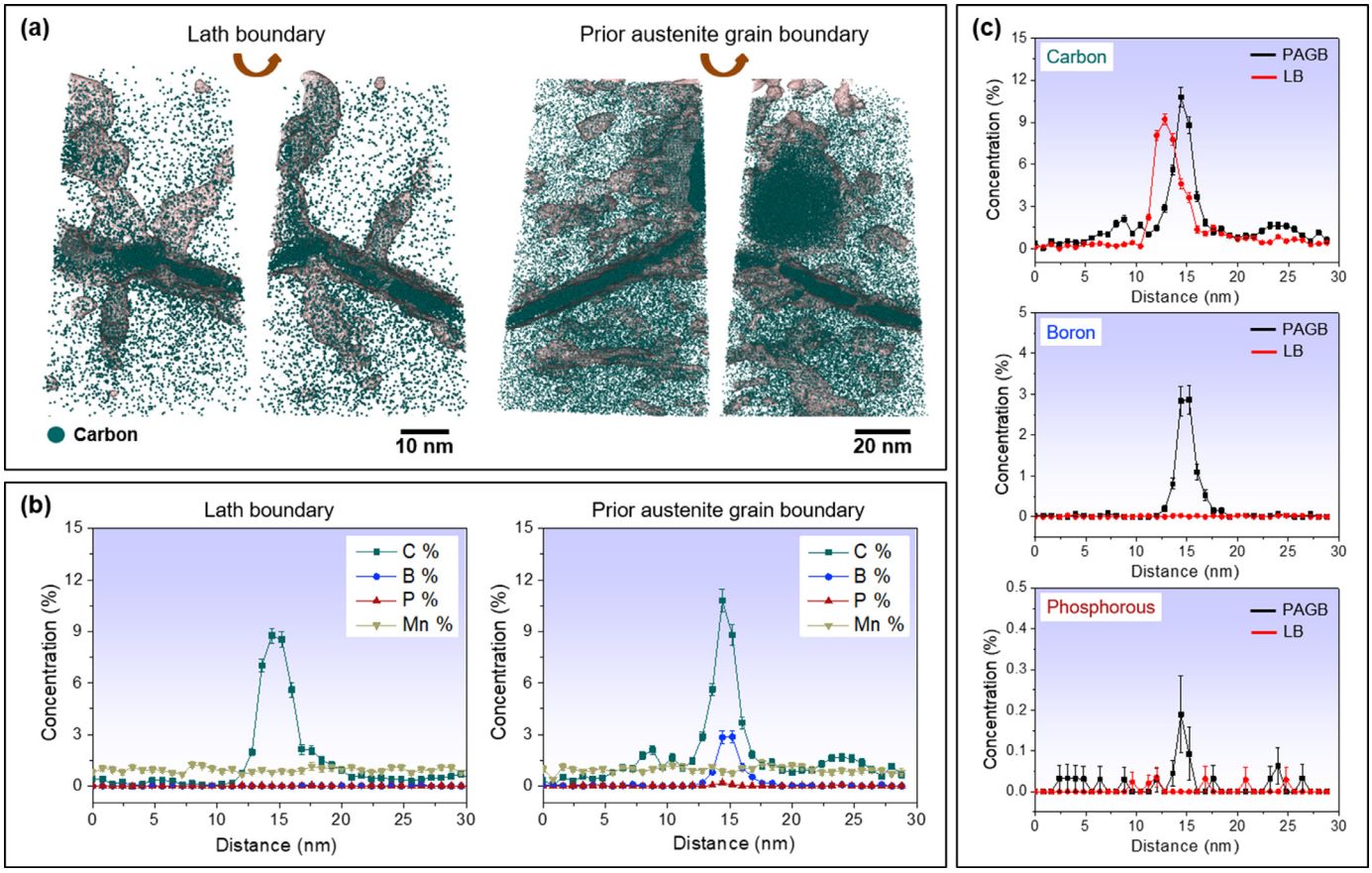

Fig. 12. APT results for the TM specimen at the lath boundary and PAGB. (a) 3D reconstruction of C distribution in each boundary. (b) Proximity histogram (proxigram) concentration profiles across the interface between the lath boundary and PAGB for C, B, P, and Mn atoms. (c) Atom concentration of C, B, and P atoms at the lath boundary and PAGB.

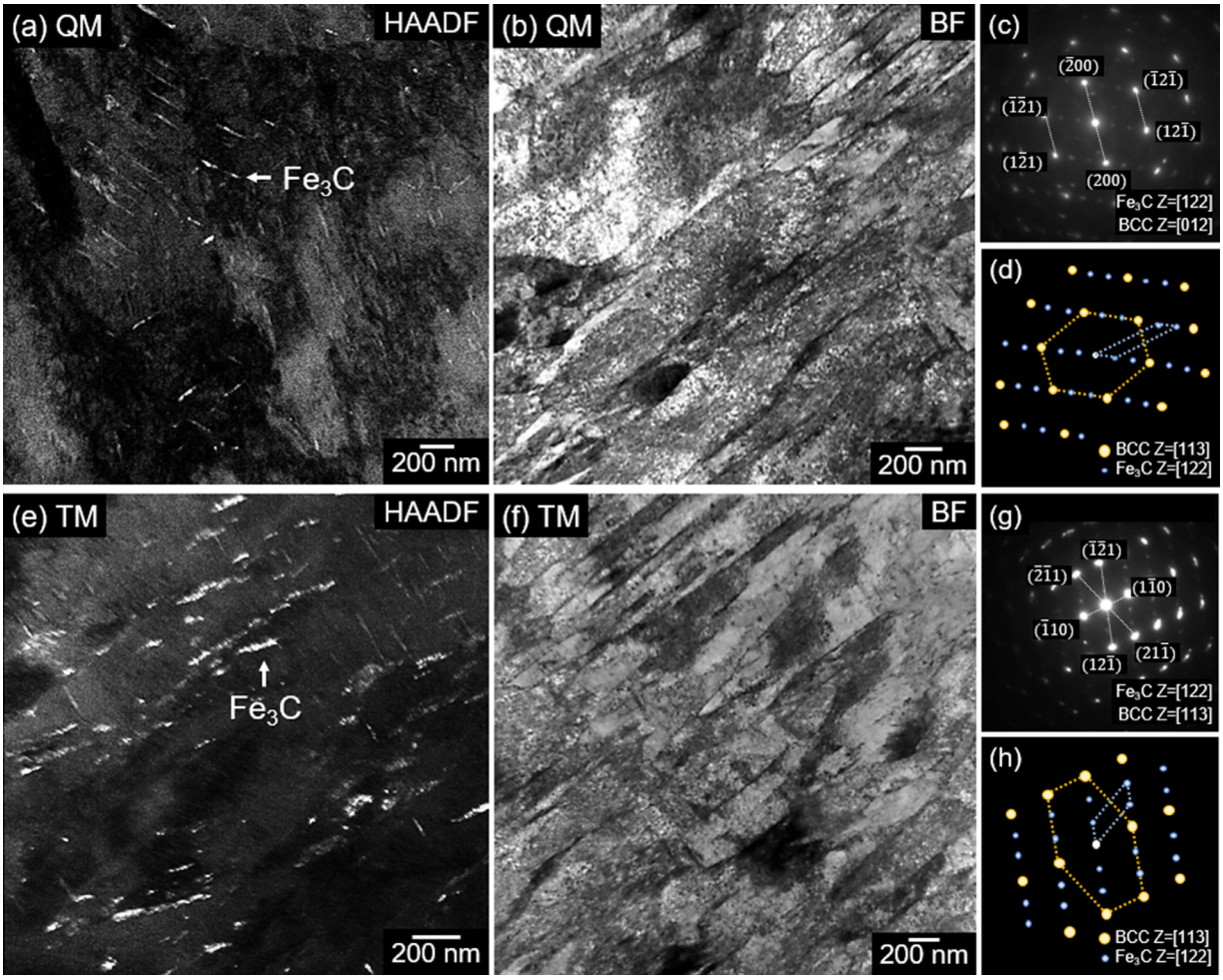

Fig. 13. TEM analysis of (a-d) QM and (e-h) TM specimens after SSRT; (a, e) high angle annular dark field (HAADF), (b, f) bright field (BF), (c, g) diffraction pattern (DP), and (d, h) schematic DPs of α-Fe and Fe_3C, showing [012] and [113] zone axes for martensite and [122] zone axis for Fe_3C. The size and density of Fe_3C (indicated by white arrows) are measured using HAADF images.

ing in crack formation at the interface between cementite and the matrix.

In Fig. 14, TEM DP analysis confirms the existence of martensite and cementite in the TM specimen. The white and gray areas in the HAADF and BF images, respectively, correspond to Fe_3C, while the black sections in both images are voids (Fig. 14(a) and (b)). In agreement with the HAADF image in Fig. 14(d), the BF image in Fig. 14(c) confirms that voids are in the vicinity of cementite particles. The TM specimen had more voids than the QM specimen due to the presence of cementites. The cementites formed along the lath boundaries and voids also appeared at the lath boundaries due to the segregation of C atoms. As previously mentioned, the segregation of B and C as solute atoms increases boundary cohesion, indicating that atomic segregation does not directly affect the boundary embrittlement. However, the segregated C atoms act as precursors of cementites, which lead to cracking at the boundary after tempering.

4.6. Combination of high strength and high resistance to SCC

Experimental verification was conducted to understand the SCC susceptibility of high-strength martensite. Notably, the misorientation angle of the lath boundary is the LAGB, while that of the block boundary is the HAGB. The packet and PAGB are also HAGB, but their misorientation angles are lower than that of the block boundary. We investigated the boundary cementites, which act as crack initiation sites in the SCC condition. In this study, microstructural factors, including the subgrain boundary itself and cementites at the boundaries, critically affect the SCC sensitivity in the high-strength martensitic steels. However, the discontinuous distribution of boundary cementites prohibit inter-lath crack propagation, thereby improving the resistance to SCC of this martensitic steel.

Fig. 15 presents a comparison of the tensile strength and corrosion potential of the martensitic steels in this study with those of other high-strength alloys. Notably, the TM and QM specimens exhibited superior corrosion resistance vs. tensile strength compared to other steels. High-strength steel has low corrosion resistance due to high dislocation density. To overcome this, we added B and controlled the tempering conditions to achieve an excellent combination of strength and corrosion resistance even in the quenched specimens. The key microstructural factor on SCC behavior is the presence of grain boundary cementites in martensitic steels. In the QM specimen, the dislocation density was negligible because tempering treatment was omitted, and cementites were scarce at the grain boundaries of the QM specimens in comparison to other martensitic steels. Thus, we tried to establish a new microstructure design strategy for developing high-strength steels. Furthermore, the QM steel exhibits high resistance to SCC despite its high dislocation density. Consequently, the sacrificing resistance to SCC is minimized relative to the enhancement of tensile strength, and the strength–SCC trade-off of high strength martensitic steels is overcome.

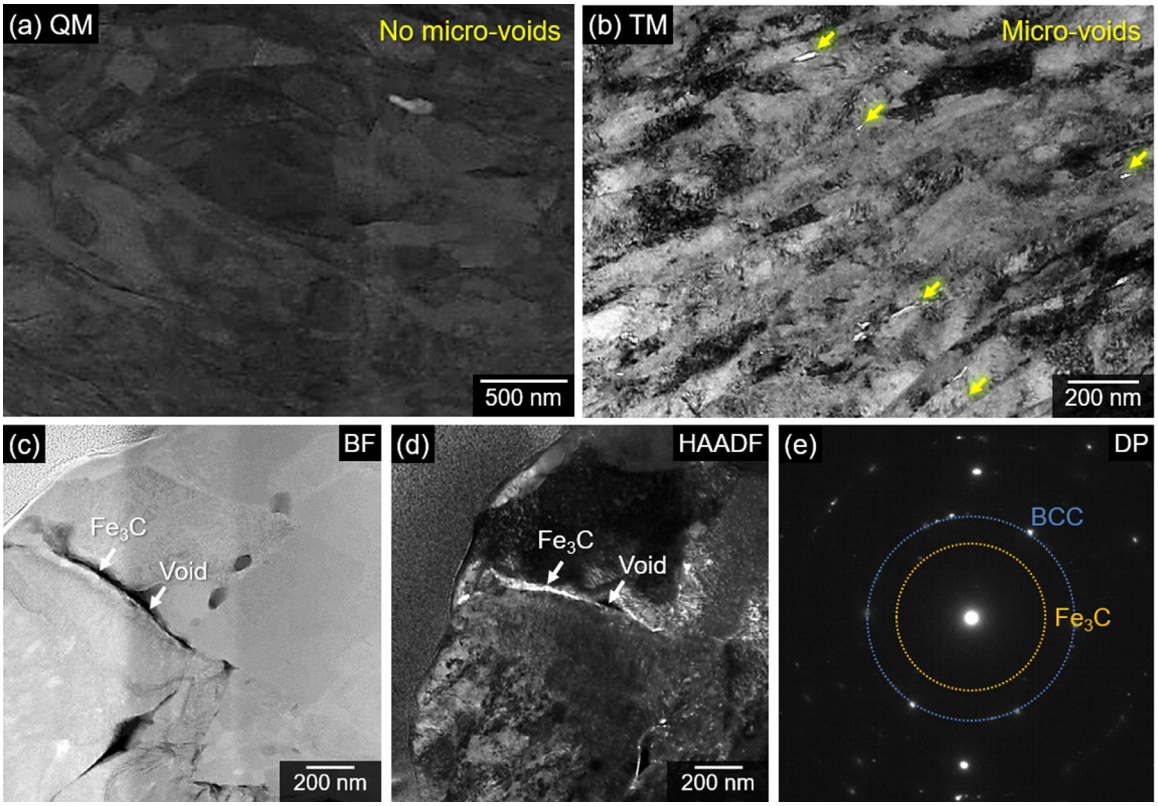

Fig. 14. TEM bright field analysis of (a) QM and (b) TM specimens after SSRT. Microvoids near Fe_3C are not obvious in the QM specimen compared to the TM specimen. (c) BF, (d) HAADF, and (e) DP analysis of TM specimen revealed the microvoids are initiated in the vicinity of Fe_3C.

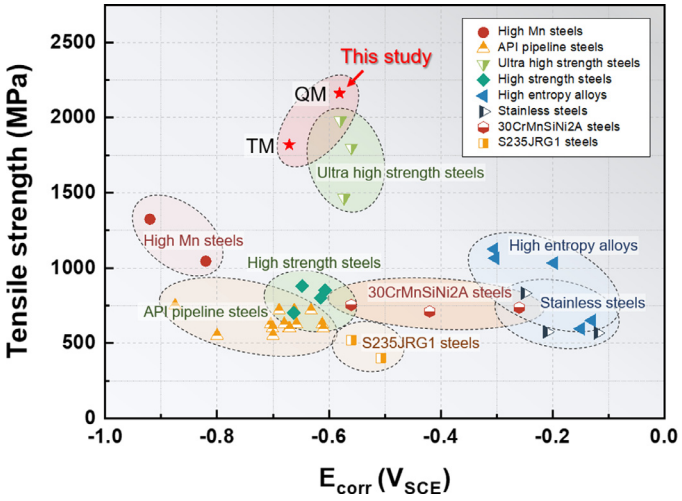

Fig. 15. Tensile and corrosion potential (E_{corr}) properties of the martensitic steel in this study were compared to those of the other high strength alloys. The strain rate ranges from 1×10^{-5} to 5×10^{-7} s^{-1} at 3.5% NaCl solution. The properties of high Mn steels [95], API pipeline steels [96–98], (ultra) high strength steels [99–101], high entropy alloys [102,103], stainless steel steels [104,105], 30CrMnSiNi2A steels [106], and S235JRG1 steels [107] are included.

5. Conclusion

This study investigated the SCC sensitivity of high-strength martensitic steels and systematically characterized their hierarchical microstructures. Microstructural factors, including subgrain boundaries and cementites, critically affect the SCC sensitivity in high-strength martensitic steels.

- We achieved an excellent combination of high tensile strength ($>$ 1.9 GPa) and high corrosion potential ($>$ −0.6 V_{SCE}) in both specimens. The QM specimens had higher strength and SCC resistance than that of the TM specimens regardless of their high GND density.
- The B atoms were mostly segregated at PAGBs, while C atoms were segregated in both PAGB and lath boundaries. These segregated atoms were precursors to cementites that acted as SCC initiation sites, revealing that C segregation affected the preferred corrosive site.
- The applications of high-strength martensitic steels in extreme environments can be expanded by understanding the different behaviors of interstitial atoms. This finding is applicable to the other metallic alloys that undergo martensitic transformation for understanding the role of complex substructures on the martensitic microstructure.

Author statement

All authors have seen and approved the final version of this manuscript being submitted. We also warrant that this article is the authors' original work, hasn't received prior publication and isn't under consideration for publication elsewhere.

We believe that this article will be of interest to the readership of your journal because it describes original and timely research of technological importance that broadly impacts industry and society in general.

This manuscript has not been published or presented elsewhere in part or in entirety and is not under consideration by another journal. We have read and understood your journal's policies, and we believe that neither the manuscript nor the study violates any of these.

Declaration of Competing Interest

The authors declare that they have no known competing financial interests or personal relationships that could have appeared to influence the work reported in this paper.

Acknowledgements

This work was supported by the National Research Foundation of Korea (NRF) grant funded by the Korea government (MSIT) (No. NRF-2020R1C1C1006214) and by the Ministry of Trade, Industry and Energy (MOTIE, Korea) under the Industrial Technology Innovation Program Grant No. 20010502. J.B.S. acknowledges financial supports from the National Research Foundation of Korea (NRF) grant funded by the Korea government (No. 2021R1A2C4002622), and from Technology Innovation Program (Alchemist Project, 1415180672, Al based supercritical materials discovery) funded by the Ministry of Trade, Industry & Energy, Korea. The authors thanks to S.H. Na for some TEM experiments and to J.H. Jang at Korea Institute of Materials Science for thermodynamic calculation.

Supplementary materials

Supplementary material associated with this article can be found, in the online version, at doi:10.1016/j.actamat.2022.118291.

References

[1] K. He, L. Wang, A review of energy use and energy-efficient technologies for the iron and steel industry, Renewable Sustainable Energy Rev. 70 (2017) 1022–1039, doi:10.1016/j.rser.2016.12.007.
[2] B.B. He, B. Hu, H.W. Yen, G.J. Cheng, Z.K. Wang, H.W. Luo, M.X. Huang, High dislocation density–induced large ductility in deformed and partitioned steels, Science 357 (2017) 1029–1032.
[3] D. Raabe, C.C. Tasan, E.A. Olivetti, Strategies for improving the sustainability of structural metals, Nature 575 (2019) 64–74, doi:10.1038/s41586-019-1702-5.
[4] B. Hu, B. He, G. Cheng, H. Yen, M. Huang, H. Luo, Super-high-strength and formable medium Mn steel manufactured by warm rolling process, Acta Mater. 174 (2019) 131–141, doi:10.1016/j.actamat.2019.05.043.
[5] W. Zhao, D. Liu, X. Zhang, Y. Zhou, R. Zhang, H. Zhang, C. Ye, Improving the fretting and corrosion fatigue performance of 300 M ultra-high strength steel using the ultrasonic surface rolling process, Int. J. Fatigue 121 (2019) 30–38, doi:10.1016/j.ijfatigue.2018.11.017.
[6] X. Guo, S. Liu, J. Xu, S. Wang, L. Fu, Z. Chai, H. Lu, Effect of step cooling process on microstructures and mechanical properties in thermal simulated CG-HAZ of an ultra-high strength steel, Mater. Sci. Eng.: A 824 (2021) 141827, doi:10.1016/j.msea.2021.141827.
[7] S. Joseph, P. Kontis, Y. Chang, Y. Shi, D. Raabe, B. Gault, D. Dye, A cracking oxygen story: a new view of stress corrosion cracking in titanium alloys, Acta Mater. 227 (2022) 117687, doi:10.1016/j.actamat.2022.117687.
[8] P. Gong, A. Turk, J. Nutter, F. Yu, B. Wynne, P. Rivera-Diaz-del-Castillo, W.Mark Rainforth, Hydrogen embrittlement mechanisms in advanced high strength steel, Acta Mater. 223 (2022) 117488, doi:10.1016/j.actamat.2021.117488.
[9] S. Ramamurthy, A. Atrens, The influence of applied stress rate on the stress corrosion cracking of 4340 and 3.5NiCrMoV steels in distilled water at 30°C, Corros. Sci. 52 (2010) 1042–1051, doi:10.1016/j.corsci.2009.11.033.
[10] W. Hao, Z. Liu, W. Wu, X. Li, C. Du, D. Zhang, Electrochemical characterization and stress corrosion cracking of E690 high strength steel in wet-dry cyclic marine environments, Mater. Sci. Eng.: A 710 (2018) 318–328, doi:10.1016/j.msea.2017.10.042.
[11] X. Xu, H. Cheng, W. Wu, Z. Liu, X. Li, Stress corrosion cracking behavior and mechanism of Fe-Mn-Al-C-Ni high specific strength steel in the marine atmospheric environment, Corros. Sci. 191 (2021) 109760, doi:10.1016/j.corsci.2021.109760.
[12] H. Li, J. Venezuela, Z. Qian, Q. Zhou, Z. Shi, M. Yan, R. Knibbe, M. Zhang, F. Dong, A. Atrens, Hydrogen fracture maps for sheared-edge-controlled hydrogen-delayed fracture of 1180 MPa advanced high-strength steels, Corros. Sci. 184 (2021) 109360, doi:10.1016/j.corsci.2021.109360.
[13] I.R. Kramer, B. Wu, C.R. Feng, Dislocation distribution in transgranular stress corrosion cracking of naval brass, Mater. Sci. Eng. 82 (1986) 141–150, doi:10.1016/0025-5416(86)90102-3.
[14] Y.H. Jang, S.S. Kim, S.Z. Han, C.Y. Lim, C.J. Kim, Corrosion and stress corrosion cracking behavior of equal channel angular pressed oxygen-free copper in 3.5% NaCl solution, J. Mater. Sci. 41 (2006) 4293–4297, doi:10.1007/s10853-006-6992-y.
[15] S. Ghosh, V.P.S. Rana, V. Kain, V. Mittal, S.K. Baveja, Role of residual stresses induced by industrial fabrication on stress corrosion cracking susceptibility of austenitic stainless steel, Mater. Des. 32 (2011) 3823–3831, doi:10.1016/j.matdes.2011.03.012.
[16] S. Cao, S. Zhu, C.V. Samuel Lim, X. Zhou, X. Chen, B.R.W. Hinton, R.R. Boyer, J.C. Williams, X. Wu, The mechanism of aqueous stress-corrosion cracking of $\alpha + \beta$ titanium alloys, Corros. Sci. 125 (2017) 29–39, doi:10.1016/j.corsci.2017.05.025.
[17] A.N. Isfahany, H. Saghafian, G. Borhani, The effect of heat treatment on mechanical properties and corrosion behavior of AISI420 martensitic stainless steel, J. Alloys Compd. 509 (2011) 3931–3936, doi:10.1016/j.jallcom.2010.12.174.
[18] S.K. Bonagani, V. Bathula, V. Kain, Influence of tempering treatment on microstructure and pitting corrosion of 13 wt.% Cr martensitic stainless steel, Corros. Sci. 131 (2018) 340–354, doi:10.1016/j.corsci.2017.12.012.
[19] Y. Wei, Y. Li, L. Zhu, Y. Liu, X. Lei, G. Wang, Y. Wu, Z. Mi, J. Liu, H. Wang, H. Gao, Evading the strength–ductility trade-off dilemma in steel through gradient hierarchical nanotwins, Nat. Commun. 5 (2014) 3580, doi:10.1038/ncomms4580.
[20] Z. Li, K.G. Pradeep, Y. Deng, D. Raabe, C.C. Tasan, Metastable high-entropy dual-phase alloys overcome the strength–ductility trade-off, Nature 534 (2016) 227–230, doi:10.1038/nature17981.
[21] Y. Liang, S. Long, P. Xu, Y. Lu, Y. Jiang, Y. Liang, M. Yang, The important role of martensite laths to fracture toughness for the ductile fracture controlled by the strain in EA4T axle steel, Mater. Sci. Eng.: A 695 (2017) 154–164, doi:10.1016/j.msea.2017.03.110.
[22] H. Kitahara, R. Ueji, N. Tsuji, Y. Minamino, Crystallographic features of lath martensite in low-carbon steel, Acta Mater. 54 (2006) 1279–1288, doi:10.1016/j.actamat.2005.11.001.
[23] Q. Li, X. Huang, W. Huang, EBSD Analysis of Relationship Between Microstructural Features and Toughness of a Medium-Carbon Quenching and Partitioning Bainitic Steel, J. Mater. Eng. Perform. 26 (2017) 6149–6157, doi:10.1007/s11665-017-3052-5.
[24] S. Long, Y. Liang, Y. Jiang, Y. Liang, M. Yang, Y. Yi, Effect of quenching temperature on martensite multi-level microstructures and properties of strength and toughness in 20CrNi2Mo steel, Mater. Sci. Eng.: A 676 (2016) 38–47, doi:10.1016/j.msea.2016.08.065.
[25] A.J. Kaijalainen, P.P. Suikkanen, T.J. Limnell, L.P. Karjalainen, J.I. Kömi, D.A. Porter, Effect of austenite grain structure on the strength and toughness of direct-quenched martensite, J. Alloys Compd. 577 (2013) S642–S648, doi:10.1016/j.jallcom.2012.03.030.
[26] W. Pitsch, The martensite transformation in thin foils of iron-nitrogen alloys, Philos. Mag. 4 (1959) 577–584.
[27] S. Zhang, S. Morito, Y. Komizo, Variant Selection of Low Carbon High Alloy Steel in an Austenite Grain during Martensite Transformation, ISIJ Int. 52 (2012) 510–515, doi:10.2355/isijinternational.52.510.
[28] C. Du, J.P.M. Hoefnagels, R. Vaes, M.G.D. Geers, Block and sub-block boundary strengthening in lath martensite, Scr. Mater. 116 (2016) 117–121, doi:10.1016/j.scriptamat.2016.01.043.
[29] C. Zhang, Q. Wang, J. Ren, R. Li, M. Wang, F. Zhang, K. Sun, Effect of martensitic morphology on mechanical properties of an as-quenched and tempered 25CrMo48V steel, Mater. Sci. Eng.: A 534 (2012) 339–346, doi:10.1016/j.msea.2011.11.078.
[30] H. Ghassemi-Armaki, R. Maaß, S.P. Bhat, S. Sriram, J.R. Greer, K.S. Kumar, Deformation response of ferrite and martensite in a dual-phase steel, Acta Mater. 62 (2014) 197–211, doi:10.1016/j.actamat.2013.10.001.
[31] T. Ohmura, A.M. Minor, E.A. Stach, J.W. Morris, Dislocation–grain boundary interactions in martensitic steel observed through in situ nanoindentation in a transmission electron microscope, J. Mater. Res. 19 (2004) 3626–3632, doi:10.1557/JMR.2004.0474.
[32] S. Morito, H. Yoshida, T. Maki, X. Huang, Effect of block size on the strength of lath martensite in low carbon steels, Mater. Sci. Eng.: A 438 (440) (2006) 237–240, doi:10.1016/j.msea.2005.12.048.
[33] D. Raabe, M. Herbig, S. Sandlöbes, Y. Li, D. Tytko, M. Kuzmina, D. Ponge, P.-.P. Choi, Grain boundary segregation engineering in metallic alloys: a pathway to the design of interfaces, Curr. Opin. Solid State Mater. Sci. 18 (2014) 253–261, doi:10.1016/j.cossms.2014.06.002.
[34] H. Ma, L. Chen, J. Zhao, Y. Huang, X. Li, Effect of prior austenite grain boundaries on corrosion fatigue behaviors of E690 high strength low alloy steel in simulated marine atmosphere, Mater. Sci. Eng.: A 773 (2020) 138884, doi:10.1016/j.msea.2019.138884.
[35] M. Kadowaki, I. Muto, H. Katayama, H. Masuda, Y. Sugawara, N. Hara, Effectiveness of an intercritical heat-treatment on localized corrosion resistance at the microstructural boundaries of medium-carbon steels, Corros. Sci. 154 (2019) 159–177, doi:10.1016/j.corsci.2019.04.019.
[36] P. Mishra, D. Yavas, A. Alshehri, P. Shrotriya, A. Bastawros, K.R. Hebert, Model of vacancy diffusion-assisted intergranular corrosion in low-alloy steel, Acta Mater. 220 (2021) 117348, doi:10.1016/j.actamat.2021.117348.
[37] J. Küpper, H. Erhart, H.-.J. Grabke, Intergranular corrosion of iron-phosphorus alloys in nitrate solutions, Corros. Sci. 21 (1981) 227–238, doi:10.1016/0010-938X(81)90032-9.
[38] A.E.S. Reyes, G.A. Guerrero, J.F.F. Álvarez, J.F.C. Alcalá, A. Salinas, I.A. Figueroa, G.L. Rodriguez, Influence of the as-cast and cold rolled microstructural conditions over corrosion resistance in an advanced TWIP steel microalloyed with boron, J. Mater. Res. Technol. 9 (2020) 4034–4043, doi:10.1016/j.jmrt.2020.02.030.

[39] N. DeCristofaro, R. Kaplow, W.S. Owen, The kinetics of carbon clustering in martensite, Metall. Trans. A 9 (1978) 821–825, doi:10.1007/BF02649791.

[40] O.N.C. Uwakweh, J.-.M. Génin, J.-.F. Silvain, Electron microscopy study of the aging and first stage of tempering of high-carbon Fe-C martensite, Metall. Trans. A 22 (1991) 797–806, doi:10.1007/BF02658989.

[41] L. Morsdorf, B. Gault, D. Ponge, C.C. Tasan, D. Raabe, Improved Atom Probe Methodology for Studying Carbon Redistribution in Low-Carbon High-Ms Lath Martensitic Steels, Microsc. Microanal. 23 (2017) 706–707, doi:10.1017/S1431927617004196.

[42] W. Lu, M. Herbig, C.H. Liebscher, L. Morsdorf, R.K.W. Marceau, G. Dehm, D. Raabe, Formation of eta carbide in ferrous martensite by room temperature aging, Acta Mater. 158 (2018) 297–312, doi:10.1016/j.actamat.2018.07.071.

[43] L. Morsdorf, E. Emelina, B. Gault, M. Herbig, C.C. Tasan, Carbon redistribution in quenched and tempered lath martensite, Acta Mater. 205 (2021) 116521, doi:10.1016/j.actamat.2020.116521.

[44] J. Li, C. Zhang, Y. Liu, Influence of carbides on the high-temperature tempered martensite embrittlement of martensitic heat-resistant steels, Mater. Sci. Eng.: A 670 (2016) 256–263, doi:10.1016/j.msea.2016.06.025.

[45] G. Gupta, P. Ampornrat, X. Ren, K. Sridharan, T.R. Allen, G.S. Was, Role of grain boundary engineering in the SCC behavior of ferritic–martensitic alloy HT-9, J. Nucl. Mater. 361 (2007) 160–173, doi:10.1016/j.jnucmat.2006.12.006.

[46] L. Wang, J. Xin, L. Cheng, K. Zhao, B. Sun, J. Li, X. Wang, Z. Cui, Influence of inclusions on initiation of pitting corrosion and stress corrosion cracking of X70 steel in near-neutral pH environment, Corros. Sci. 147 (2019) 108–127, doi:10.1016/j.corsci.2018.11.007.

[47] L. Wang, C. Dong, C. Man, Y. Hu, Q. Yu, X. Li, Effect of microstructure on corrosion behavior of high strength martensite steel—a literature review, Int. J. Minerals Metallurgy Mater. 28 (2021) 754–773, doi:10.1007/s12613-020-2242-6.

[48] H.B. Xue, Y.F. Cheng, Characterization of inclusions of X80 pipeline steel and its correlation with hydrogen-induced cracking, Corros. Sci. 53 (2011) 1201–1208, doi:10.1016/j.corsci.2010.12.011.

[49] H. Ezuber, A. Alshater, S.O. Nisar, A. Gonsalvez, S. Aslam, Effect of surface finish on the pitting corrosion behavior of sensitized AISI 304 austenitic stainless steel alloys in 3.5% NaCl solutions, Surf. Eng. Appl. Electrochem. 54 (2018) 73–80, doi:10.3103/S1068375518010039.

[50] D.S. Qian, X.L. Zhong, T. Hashimoto, Y.Z. Yan, Z. Liu, Effect of excimer laser surface melting on the corrosion performance of a SiCp/Al metal matrix composite, Appl. Surf. Sci. 330 (2015) 280–291, doi:10.1016/j.apsusc.2014.12.132.

[51] M.S.N. Bhat, M.K. Surappa, H.S. Nayak, Corrosion behaviour of silicon carbide particle reinforced 6061/Al alloy composites, J. Mater. Sci. 26 (1991) 4991–4996, doi:10.1007/BF00549882.

[52] I.B. Singh, D.P. Mandal, M. Singh, S. Das, Influence of SiC particles addition on the corrosion behavior of 2014 Al–Cu alloy in 3.5% NaCl solution, Corros. Sci. 51 (2009) 234–241, doi:10.1016/j.corsci.2008.11.001.

[53] ASTM InternationalASTM E8/E8M-16a: Standard Test Methods for Tension Testing of Metallic Materials, ASTM International, West Conshohocken, PA, USA, 2016.

[54] A.S.T.M. International, ASTM G5-94: Standard Reference Test Method For Making Potentiostatic and Potentiodynamic Anodic Polarization Measurements, ASTM International, West Conshohocken, PA, USA, 2011.

[55] J.B. Seol, D. Haley, D.T. Hoelzer, J.H. Kim, Influences of interstitial and extrusion temperature on grain boundary segregation, Y–Ti–O nanofeatures, and mechanical properties of ferritic steels, Acta Mater. 153 (2018) 71–85, doi:10.1016/j.actamat.2018.04.046.

[56] J.B. Seol, G.H. Gu, S.L. Nam, S. Das, C.H. Park, Atomic scale investigation on the distribution of boron in medium carbon steels by atom probe tomography and EELS, Ultramicroscopy 110 (2010) 783–788, doi:10.1016/j.ultramic.2009.12.006.

[57] B.P.J. Sandvik, C.M. Wayman, Characteristics of lath martensite: part I. Crystallographic and substructural features, Metall. Trans. A 14 (1983) 809–822, doi:10.1007/BF02644284.

[58] J.P. Miles, Bifurcation in plastic flow under uniaxial tension, J. Mech. Phys. Solids 19 (1971) 89–102, doi:10.1016/0022-5096(71)90020-2.

[59] J.W. Hutchinson, J.P. Miles, Bifurcation analysis of the onset of necking in an elastic/plastic cylinder under uniaxial tension, J. Mech. Phys. Solids 22 (1974) 61–71, doi:10.1016/0022-5096(74)90014-3.

[60] J.A. Rodríguez-Martínez, D. Rittel, R. Zaera, S. Osovski, Finite element analysis of AISI 304 steel sheets subjected to dynamic tension: the effects of martensitic transformation and plastic strain development on flow localization, Int. J. Impact Eng. 54 (2013) 206–216, doi:10.1016/j.ijimpeng.2012.11.003.

[61] ASTM InternationalASTM G3-14: Standard Practice For Conventions Applicable to Electrochemical Measurements in Corrosion Testing, ASTM International, West Conshohocken, PA, USA, 2019.

[62] A. Wiengmoon, T. Chairuangsri, A. Brown, R. Brydson, D.V. Edmonds, J.T.H. Pearce, Microstructural and crystallographical study of carbides in 30 wt.%Cr cast irons, Acta Mater. 53 (2005) 4143–4154, doi:10.1016/j.actamat.2005.05.019.

[63] B. Qin, Z.Y. Wang, Q.S. Sun, Effect of tempering temperature on properties of 00Cr16Ni5Mo stainless steel, Mater. Charact. 59 (2008) 1096–1100, doi:10.1016/j.matchar.2007.08.025.

[64] Y. Jang, S. Kim, J. Lee, Effect of different Mo contents on tensile and corrosion behaviors of CD4MCU cast duplex stainless steels, Metall. Mater. Trans. A 36 (2005) 1229–1236, doi:10.1007/s11661-005-0215-z.

[65] H. Lee, Y. Kim, Y. Jeong, S. Kim, Effects of testing variables on stress corrosion cracking susceptibility of Al 2024-T351, Corros. Sci. 55 (2012) 10–19, doi:10.1016/j.corsci.2011.09.021.

[66] M. Calcagnotto, D. Ponge, E. Demir, D. Raabe, Orientation gradients and geometrically necessary dislocations in ultrafine grained dual-phase steels studied by 2D and 3D EBSD, Mater. Sci. Eng.: A 527 (2010) 2738–2746, doi:10.1016/j.msea.2010.01.004.

[67] F.R.N. Nabarro, Z.S. Basinski, D.B. Holt, The plasticity of pure single crystals, Adv. Phys. 13 (1964) 193–323, doi:10.1080/00018736400101031.

[68] S.C. Kennett, G. Krauss, K.O. Findley, Prior austenite grain size and tempering effects on the dislocation density of low-C Nb–Ti microalloyed lath martensite, Scr. Mater. 107 (2015) 123–126, doi:10.1016/j.scriptamat.2015.05.036.

[69] D. Kuhlmann-Wilsdorf, Theory of plastic deformation: - properties of low energy dislocation structures, Mater. Sci. Eng.: A 113 (1989) 1–41, doi:10.1016/0921-5093(89)90290-6.

[70] L. Morsdorf, O. Jeannin, D. Barbier, M. Mitsuhara, D. Raabe, C.C. Tasan, Multiple mechanisms of lath martensite plasticity, Acta Mater. 121 (2016) 202–214, doi:10.1016/j.actamat.2016.09.006.

[71] L. Morsdorf, C.C. Tasan, D. Ponge, D. Raabe, 3D structural and atomic-scale analysis of lath martensite: effect of the transformation sequence, Acta Mater. 95 (2015) 366–377, doi:10.1016/j.actamat.2015.05.023.

[72] M. Kuzmina, D. Ponge, D. Raabe, Grain boundary segregation engineering and austenite reversion turn embrittlement into toughness: example of a 9 wt.% medium Mn steel, Acta Mater. 86 (2015) 182–192, doi:10.1016/j.actamat.2014.12.021.

[73] Y.F. Jiang, W. Xu, Q. Zhang, B. Zhang, Improvement of hydrogen embrittlement resistance by intense pulsed ion beams for a martensitic steel, Int. J. Hydrogen Energy 46 (2021) 21239–21248, doi:10.1016/j.ijhydene.2021.03.193.

[74] R. Wu, A.J. Freeman, G.B. Olson, Effects of carbon on Fe-grain-boundary cohesion: first-principles determination, Phys. Rev. B 53 (1996) 7504–7509, doi:10.1103/PhysRevB.53.7504.

[75] P. Lejček, S. Hofmann, V. Paidar, Solute segregation and classification of [100]tilt grain boundaries in α-iron: consequences for grain boundary engineering, Acta Mater. 51 (2003) 3951–3963, doi:10.1016/S1359-6454(03)00219-2.

[76] R. Yang, D.L. Zhao, Y.M. Wang, S.Q. Wang, H.Q. Ye, C.Y. Wang, Effects of Cr, Mn on the cohesion of the γ-iron grain boundary, Acta Mater. 49 (2001) 1079–1085, doi:10.1016/S1359-6454(00)00382-7.

[77] R. Yang, Y.M. Wang, R.Z. Huang, H.Q. Ye, C.Y. Wang, First-principles study on the effect of Mn and N on the cohesion of a γ-iron grain boundary, Phys. Rev. B 65 (2002) 094112, doi:10.1103/PhysRevB.65.094112.

[78] M.P. Seah, Adsorption-induced interface decohesion, Acta Metall. 28 (1980) 955–962, doi:10.1016/0001-6160(80)90112-1.

[79] R.P. Messmer, C.L. Briant, The role of chemical bonding in grain boundary embrittlement, Acta Metall. 30 (1982) 457–467, doi:10.1016/0001-6160(82)90226-7.

[80] L. Zhong, R. Wu, A.J. Freeman, G.B. Olson, Effects of Mn additions on the P embrittlement of the Fe grain boundary, Phys. Rev. B 55 (1997) 11133–11137, doi:10.1103/PhysRevB.55.11133.

[81] W.T. Geng, A.J. Freeman, G.B. Olson, Influence of alloying additions on grain boundary cohesion of transition metals: first-principles determination and its phenomenological extension, Phys. Rev. B 63 (2001) 165415.

[82] D. McLean, A. Maradudin, Grain boundaries in metals, Phys. Today 11 (1958) 35.

[83] S. Shenhua, X. Tingdong, Combined equilibrium and non-equilibrium segregation mechanism of temper embrittlement, J. Mater. Sci. 29 (1994) 61–66, doi:10.1007/BF00356573.

[84] P. Lejček, Principles of Non-equilibrium Segregation, in: P. Lejcek (Ed.), Grain Boundary Segregation in Metals, Springer, Berlin, Heidelberg, 2010, pp. 153–171, doi:10.1007/978-3-642-12505-8_6.

[85] C. Guo, P.M. Kelly, Boron solubility in Fe–Cr–B cast irons, Mater. Sci. Eng.: A 352 (2003) 40–45, doi:10.1016/S0921-5093(02)00449-5.

[86] D.A. Basha, R. Sahara, H. Somekawa, A. Singh, K. Tsuchiya, Effect of processing strain rate and temperature on interfacial segregation of zinc in a magnesium alloy, Mater. Sci. Eng.: A 703 (2017) 54–67, doi:10.1016/j.msea.2017.07.041.

[87] J. Takahashi, K. Ishikawa, K. Kawakami, M. Fujioka, N. Kubota, Atomic-scale study on segregation behavior at austenite grain boundaries in boron- and molybdenum-added steels, Acta Mater. 133 (2017) 41–54, doi:10.1016/j.actamat.2017.05.021.

[88] R.G. Faulkner, Non-equilibrium grain-boundary segregation in austenitic alloys, J. Mater. Sci. 16 (1981) 373–383, doi:10.1007/BF00738626.

[89] G. Miyamoto, A. Goto, N. Takayama, T. Furuhara, Three-dimensional atom probe analysis of boron segregation at austenite grain boundary in a low carbon steel - Effects of boundary misorientation and quenching temperature, Scr. Mater. 154 (2018) 168–171, doi:10.1016/j.scriptamat.2018.05.046.

[90] X. Tingdong, C. Buyuan, Kinetics of non-equilibrium grain-boundary segregation, Prog. Mater Sci. 49 (2004) 109–208, doi:10.1016/S0079-6425(03)00019-7.

[91] W. Wang, S. Zhang, X. He, Diffusion of boron in alloys, Acta Metall. Mater. 43 (1995) 1693–1699, doi:10.1016/0956-7151(94)00347-K.

[92] M. Ollat, M. Militzer, V. Massardier, D. Fabregue, E. Buscarlet, F. Keovilay, M. Perez, Mixed-mode model for ferrite-to-austenite phase transformation in dual-phase steel, Comput. Mater. Sci. 149 (2018) 282–290, doi:10.1016/j.commatsci.2018.02.052.

[93] E. de Smit, F. Cinquini, A.M. Beale, O.V. Safonova, W. van Beek, P. Sautet, B.M. Weckhuysen, Stability and Reactivity of $\epsilon-\chi-\theta$ Iron Carbide Catalyst

Phases in Fischer–Tropsch Synthesis: controlling μC, J. Am. Chem. Soc. 132 (2010) 14928–14941, doi:10.1021/ja105853q.
[94] Q. Chang, C. Zhang, C. Liu, Y. Wei, A.V. Cheruvathur, A.I. Dugulan, J.W. Niemantsverdriet, X. Liu, Y. He, M. Qing, L. Zheng, Y. Yun, Y. Yang, Y. Li, Relationship between Iron Carbide Phases (ε-Fe2C, Fe7C3, and χ-Fe5C2) and Catalytic Performances of Fe/SiO2 Fischer–Tropsch Catalysts, ACS Catal 8 (2018) 3304–3316, doi:10.1021/acscatal.7b04085.
[95] H. Choi, S. Kim, H. Sung, S. Kim, S. Kim, Effect of Cr and N on Stress Corrosion Cracking Behavior of Fe-18Mn Steel, Korean J. Metals Mater. 57 (2019) 624–631.
[96] P.C. Okonkwo, F. Ahmad, B. Hossein, Effect of Muscat Oilfield Brine on the Stressed X-70 Pipeline Steel, Vacuum 164 (2019) 126–131, doi:10.1016/j.vacuum.2019.03.013.
[97] C.H. Lin, Characterization of SPCC Steel Stress Behaviour in Brine Water Environment, Int. J. Electrochem. Sci. 14 (2019) 2321–2332, doi:10.20964/2019.03.26.
[98] H. Wang, C. Yu, S. Huang, Effect of heat treatment on mechanical property and electrochemical corrosion behavior of X65 pipeline steel in 3.5 wt.% NaCl, Int. J. Electrochem. Sci. 10 (2015) 5827–5841.
[99] J. Chen, Y. Yang, L. Li, Z. Wang, H. Xiao, Y. Wei, T. Zhu, H. Sun, Effects of Ti on Microstructure, Mechanical Properties and Corrosion Behavior of High-Strength Steel Weld Metals for Offshore Structures, Int. J. Electrochem. Sci. 16 (2021), doi:10.20964/2021.08.36.
[100] J. Liu, K. Zhao, M. Yu, S. Li, C. Wen, Effect of Electrochemical Potential and Chloride Concentration on Stress Corrosion Cracking Behavior of 23Co14Ni12Cr3Mo Ultra-High Strength Steel in NaCl Solution, Int. J. Electrochem. Sci. 9 (2014) 3246–3258.
[101] Q. Guo, J. Liu, M. Yu, S. Li, Comparative Evaluations on Stress Corrosion Cracking Mechanism of Low Alloy Ultra-High Strength Steels in Neutral 3.5 wt% NaCl Solution, Int. J. Electrochem. Sci. 10 (2015) 701–712.
[102] S.S. Nene, M. Frank, K. Liu, S. Sinha, R.S. Mishra, B.A. McWilliams, K.C. Cho, Corrosion-resistant high entropy alloy with high strength and ductility, Scr. Mater. 166 (2019) 168–172, doi:10.1016/j.scriptamat.2019.03.028.
[103] P. Varshney, R.S. Mishra, N. Kumar, Stress Corrosion Cracking of TRIP Fe39Mn20Co20Cr15Si5Al1 (at.%) High Entropy Alloy, in: TMS 2021 150th Annual Meeting & Exhibition Supplemental Proceedings, 2021, pp. 742–750, doi:10.1007/978-3-030-65261-6_67.
[104] C. Zhang, J. Zhu, C. Ji, Y. Guo, R. Fang, S. Mei, S. Liu, Laser powder bed fusion of high-entropy alloy particle-reinforced stainless steel with enhanced strength, ductility, and corrosion resistance, Mater. Des. 209 (2021) 109950, doi:10.1016/j.matdes.2021.109950.
[105] T. Ron, O. Dolev, A. Leon, A. Shirizly, E. Aghion, Effect of Phase Transformation on Stress Corrosion Behavior of Additively Manufactured Austenitic Stainless Steel Produced by Directed Energy Deposition, Materials (Basel) 14 (2021) 55, doi:10.3390/ma14010055.
[106] J. Liu, Q. Guo, M. Yu, L. Songmei, SCC investigation of low alloy ultra-high strength steel 30CrMnSiNi2A in 3.5wt% NaCl solution by slow strain rate technique, Chin. J. Aeronaut. 27 (2014) 1327–1333, doi:10.1016/j.cja.2014.03.025.
[107] P. Zagożdżon, R. Starosta, Influence of Seawater Salinity on Corrosion of Hull Structural Steel, J. KONES 26 (2019) 189–195, doi:10.2478/kones-2019-0049.